Tectonics®

RESEARCH ARTICLE
10.1029/2023TC008139

Block Rotations in NW Iran in Response to the Arabia-Eurasia Collision Constrained by Paleomagnetism

Ali Niknam[1], Annique van der Boon[2], Mahnaz Rezaeian[1], Nuretdin Kaymakcı[3], and Cor Langereis[4]

[1]Department of Earth Sciences, Institute for Advanced Studies in Basic Sciences, Zanjan, Iran, [2]Centre for Planetary Habitability, University of Oslo, Oslo, Norway, [3]Department of Geological Engineering, Middle East Technical University, Ankara, Türkiye, [4]Paleomagnetic Laboratory Fort Hoofddijk, Utrecht University, Utrecht, The Netherlands

Abstract Northwest Iran is a seismically active region dominated by NW-SE trending strike-slip faults, such as the North Tabriz and Qosha Dagh faults, and smaller NNE-SSW striking faults. The Bozgush Mountains are shaped by these faults and divided into two domains that show a difference in strike. To quantify rotational tectonic deformation in NW Iran, we performed a paleomagnetic study along three transects of the Bozgush and Qosha Dagh Mountains with 127 sites. Our large new paleomagnetic data set shows that the Bozgush Mountains did not rotate as a single rigid block. In the western domain of the Bozgush Mountains, we find evidence for clockwise vertical axis rotations of ~40°, while the eastern domain has rotated up to ~80° clockwise. Declinations of the western Bozgush domain fit well with observed declinations in the Qosha Dagh Mountains. Fault patterns show that the eastern domain of the Bozgush Mountains is divided by a set of NNE-SSW striking sinistral strike-slip faults, which created domino-style blocks that accommodated the additional 40° of rotation. We estimate that these extra rotations have resulted in around 4 km of N-S shortening and more than 1.5 km of differential uplift.

Plain Language Summary This study focuses on the tectonic history of northwest Iran, specifically the Bozgush and Qosha Dagh Mountains. Northwest Iran is prone to destructive earthquakes and hosts large strike-slip faults, including the North Tabriz and Qosha Dagh faults. We conducted a paleomagnetic study to understand how these faults are linked to rotations of crustal blocks. We found that the Bozgush Mountains did not rotate as a single rigid block. The western Bozgush domain has rotated clockwise by about 40°, while the eastern domain has rotated much more, around 80° clockwise. The eastern domain is cross-cut by a distinct set of NNE-SSW striking left-lateral faults, while the western domain does not have similar faults. These faults are active today and are linked to earthquakes.

1. Introduction

The northwest of Iran is a seismically very active region with densely populated cities (e.g., Tabriz; population >1.5 million, Ardabil; population >0.5 million) prone to seismic hazard. Understanding the geological characteristics of this region is crucial in term of earthquake awareness and mitigation. Although there are a large number of studies addressing issues such as paleoseismicity (Berberian, 1997; Hessami et al., 2003), geohazards (Berberian & Arshadi, 1976; Copley et al., 2014; Ghods et al., 2015), and morphotectonics (Faridi et al., 2017; Rizza et al., 2013; Saber et al., 2018; Solaymani Azad et al., 2015), studies addressing the tectonic development and rotational deformation in the region are lacking.

Northwest Iran is cut by several major active right-lateral strike slip faults (Figure 1) with a roughly NW-SE orientation; the largest of which is the Tabriz fault system. Also large left-lateral strike-skip faults are present, with a NE-SW orientation, such as the Aras fault (Saber et al., 2021). Additionally, there is a set of smaller, active, left-lateral strike slip faults, which are conjugate to the larger right-lateral faults (Faridi et al., 2017). These faults cross-cut the large right-lateral faults in places, and have orientations that are roughly NNE-SSW (Figure 1a). Our study focuses on the Bozgush and Qosha Dagh areas in NW Iran (Figure 1). Structurally, the area lies adjacent to the Z-shaped Lesser Caucasus-Talesh-Alborz-Kopeh Dagh Orocline (Rezaeian et al., 2020). The Bozgush Mountains are a roughly E-W trending high with an average altitude of around 3 km, bounded by the North and South Bozgush faults (Figure 1). These are two major seismically active dextral faults striking NW-SE to E-W. Toward the east, the faults become dextral strike-slip faults with reverse components (Faridi et al., 2017). The South Bozgush fault is the locus of a large historical earthquake of M_w 6.7 that occurred in 1879 and resulted in

Ali Niknam and Annique van der Boon contributed equally to this work (Shared first authorship).

Key Points:

- Paleomagnetic data show evidence for a ~40° regional clockwise rotation since the Eocene, in response to the Arabia-Eurasia collision
- E and W Bozgush domains show different amounts of rotation, with those in the E domain twice as large (80°) as in the W domain
- Rotations in the east Bozgush domain are accommodated by a set of extra faults, of which some are linked to recent destructive earthquakes

Supporting Information:

Supporting Information may be found in the online version of this article.

Correspondence to:

A. van der Boon,
a.van.der.boon@geo.uio.no

Citation:

Niknam, A., van der Boon, A., Rezaeian, M., Kaymakcı, N., & Langereis, C. (2024). Block rotations in NW Iran in response to the Arabia-Eurasia collision constrained by paleomagnetism. *Tectonics*, *43*, e2023TC008139. https://doi.org/10.1029/2023TC008139

Received 9 OCT 2023
Accepted 18 JUL 2024

Author Contributions:

Conceptualization: Ali Niknam, Annique van der Boon, Mahnaz Rezaeian, Nuretdin Kaymakcı, Cor Langereis
Data curation: Ali Niknam, Annique van der Boon, Cor Langereis
Formal analysis: Ali Niknam, Annique van der Boon, Cor Langereis
Funding acquisition: Cor Langereis
Investigation: Ali Niknam, Annique van der Boon, Mahnaz Rezaeian, Nuretdin Kaymakcı, Cor Langereis

Methodology: Ali Niknam, Annique van der Boon, Mahnaz Rezaeian, Cor Langereis
Project administration: Mahnaz Rezaeian, Cor Langereis
Supervision: Annique van der Boon, Mahnaz Rezaeian, Cor Langereis
Validation: Annique van der Boon, Nuretdin Kaymakcı, Cor Langereis
Visualization: Nuretdin Kaymakcı, Cor Langereis
Writing – original draft: Ali Niknam, Annique van der Boon, Nuretdin Kaymakcı, Cor Langereis
Writing – review & editing: Annique van der Boon, Mahnaz Rezaeian, Nuretdin Kaymakcı, Cor Langereis

more than 2,000 casualties (Valerio et al., 2020). The eastern domain of the Bozgush Mountains is cut by a set of NNE-SSW striking sinistral strike-slip faults (Faridi et al., 2017). These faults are also responsible for destructive earthquakes, the most recent of which took place in November 2019, with a magnitude of M_w: 5.9 within the middle of the Bozgush range (Isik et al., 2021; Valerio et al., 2020; Yang et al., 2020). This event caused the loss of several lives and destruction of many houses. Another large earthquake occurred in this region >400 years ago (1593 AD, $M = 6$, $I_0 =$ VIII; Solaymani Azad et al., 2019a).

Contrary to the general trend of the Lesser Caucasus-Talesh-Alborz-Kopeh Dagh Orocline (Rezaeian et al., 2020; van der Boon et al., 2018), the Bozgush Mountains follow a WNW-ESE strike which becomes WSW-ENE further east, almost perpendicular to the orocline. The rock units exposed within the Bozgush Mountains comprise mainly Eocene volcanic rocks and there is a conspicuous difference in strike between the western and eastern domains; the western domain has an approximate trend of 105N while the eastern domain trends almost 070N. The hinge-line between the western and eastern domains is the Shalgun-Yelimsi fault (SYF in Figure 1a). The eastern domain is traversed by numerous NNE-SSW striking sinistral strike-slip faults while the western domain seems to be intact and does not contain similar strike-slip faults (Faridi et al., 2017) with the exception of the left-lateral Bostanabad fault (BAF in Figure 1a). The Bozgush Mountains rise more than 1.5 km above the surrounding Iranian plateau, forming a positive flower structure (Faridi et al., 2017). Faridi et al. (2017) have suggested that the eastern Bozgush domain has rotated around 30° counter-clockwise (CCW) with respect to the western Bozgush domain, apparently based on the morphotectonics, that is, the difference in the strikes (105–70N = 35° CCW).

Although considerable research has been devoted to unravel the structural geological and seismotectonic characteristics of the area, the relationship between the structures and possible rotations in the area has received much less attention. In this contribution, we aim to unravel the kinematic link between the observed structures and style of deformation in the Bozgush Mountains, based on paleomagnetic data that provide information about the sense and amount of vertical axis rotations in the region.

1.1. Geological Setting

Northwest Iran is situated within the Alpine-Himalayan orogenic belt, and is the locus of the central portion of the convergence zone between the Arabian and Eurasian plates (Jackson, 1992). The region has been subjected to overall N-S shortening and E-W extension manifested by complex faulting, earthquakes and Cenozoic-Quaternary volcanic activity (Faridi et al., 2017). Recent Global Navigation Satellite System (GNSS)-based measurements indicate that Arabia-Eurasia convergence occurs at a rate of about 20–30 mm/year (Reilinger et al., 2006; Vernant et al., 2004). On the other hand, geological and paleoseismological studies in NW Iran offer relatively slower rates of 6–8 mm/year (Djamour et al., 2011; Hessami et al., 2003).

One of the main structures in NW Iran is the dextral Tabriz fault which extends to the northwest along the Gailatu-Siah Cheshmeh-Khoy (GSKF) fault which continues further west in to Türkiye and links up with the Çaldıran fault system (ÇF; Figure 1). The throughgoing, relatively straight part of the Tabriz fault is more than 150 km long. On its eastern and western ends, the Tabriz fault terminates with restraining bends, where the fault becomes an almost E-W striking dextral fault with a reverse component (the South Misho fault; SMF in Figure 1 and eastern domain of the Bozgush mountain ranges, respectively; Figure 1). The Tabriz fault Zone is an active fault zone that has historically produced various devastating earthquakes, although it has been quiet for more than a century (Berberian & Arshadi, 1976). Watson et al. (2024) report present-day right-lateral slip rates on the North Tabriz fault (NTF) of 8–10 mm/year.

To the east of Bostanabad, the Tabriz fault zone widens gradually in a well-defined, fault-bounded positive topography along which the throughgoing strike-slip fault character gradually changes into strike-slip fault with a reverse component (transpression) toward its eastern termination (Saber et al., 2018). The change in character is accommodated by bifurcation of the fault zone into two major faults delimiting the Bozgush Mountains. The northern branch dips southwards while the southern branch dips northwards, and they both have dextral strike-slip characters with a reverse component. These faults accommodate the transpressional deformation resulting from gradual bending of the fault zone northwards, which resulted in the rise of the Bozgush Mountains as a positive flower structure. Currently, however, the Bozgush Mountains are undergoing extension, rather than compression (Djamour et al., 2011). The Bozgush range reaches up to 3,200 m altitude and rises more than 1,500 m above the surrounding lowlands. The curvature of the range, hence the reverse component and altitude, increases gradually toward the east. At its eastern end, the Bozgush Mountains are delimited by the dextral Sendan-Seyedlar fault.

10.1029/2023TC008139

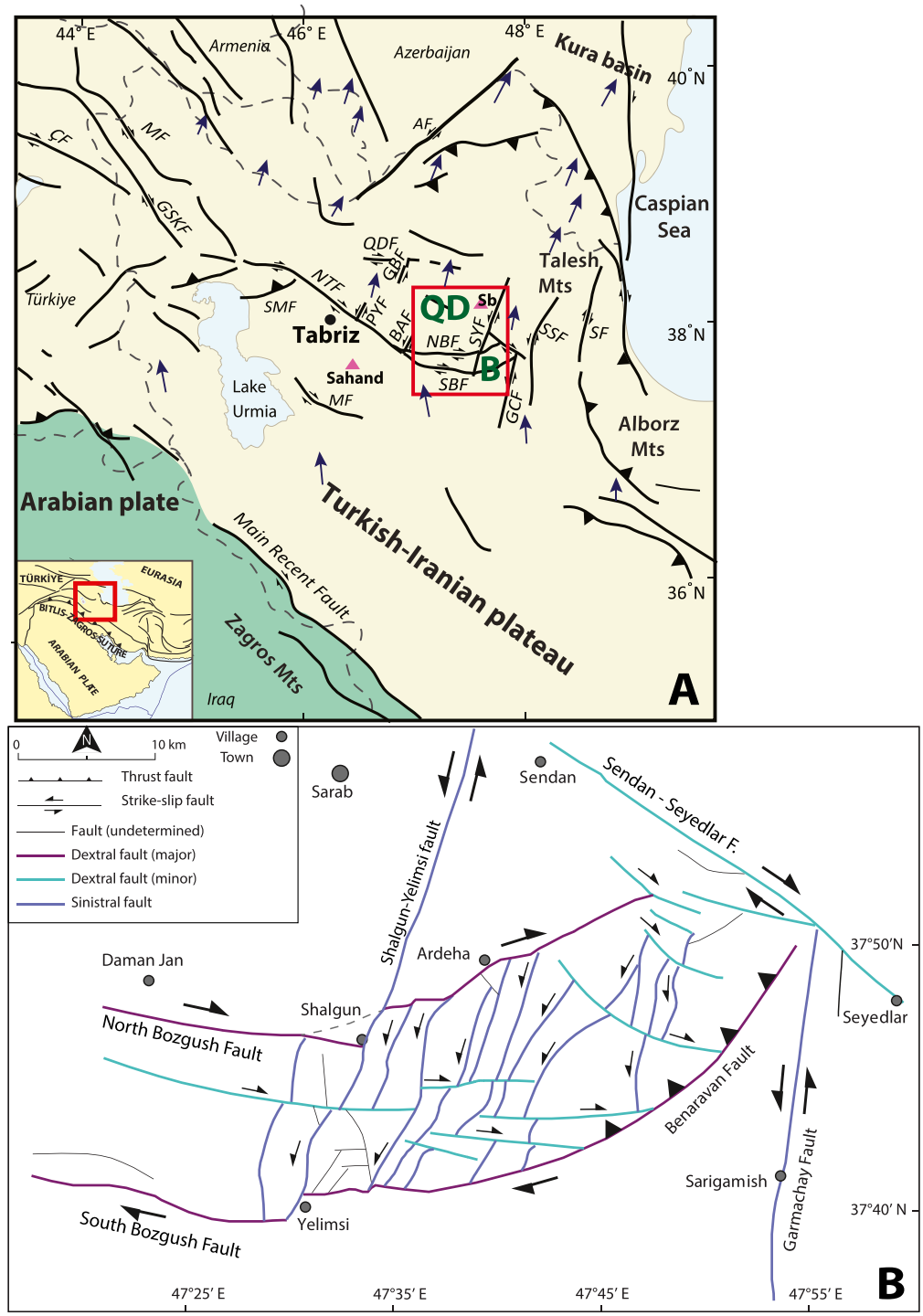

Figure 1. (a) Map of the Northwest Iranian plateau with study area (red box), plate boundaries and faults (modified after Faridi et al., 2017; Saber et al., 2018). B, Bozgush; QD, Qosha Dagh; Sb, Sabalan volcano; AF, Aras fault; BAF, Bostanabad fault; ÇF, Çaldıran fault; GBF, Guyjabel fault; GCF, Garmachay fault; GSKF, Gailatu-Siah Cheshmeh-Khoy fault; MF, Maragheh fault; NTF, North Tabriz fault; NBF, North Bozgush fault; QDF, Qosha Dagh fault; SBF, South Bozgush fault; SF, Sangavan fault; SMF, South Misho fault; SYF, Shalgun-Yelimsi fault; SSF, Sendan-Seyyedlar fault; PYF, Payan fault. Global Positioning System (GPS) velocity vectors (arrows) from Djamour et al. (2011), Reilinger et al. (2006). (b) Faults in the Bozgush region, modified from Faridi et al. (2017). The North and South Bozgush faults are major dextral faults, and likely belong to the same fault population as the minor dextral faults. The sinistral faults have a different orientation and accommodate additional clockwise rotations.

Within the Bozgush Mountains, there are several NNE-striking sinistral active seismogenic faults, such as the Shalgun-Yelimsi and Garmachay faults, that intersect the E-striking oblique-dextral faults (Figure 1). Furthermore, the eastern limb of the Bozgush Mountains is cut by many NNE-SSW striking sinistral faults, which are not present to the same extent in the western limb of the Bozgush Mountains (Figure 1b). The 8 November 2019 earthquake in NW Iran affected the central part of the East Bozgush range and was reported to have no direct relation to the NTF. Solaymani Azad et al. (2019b) and Valerio et al. (2020) suggested that the NNE-striking SYF fault (Faridi et al., 2017; Figure 1) is the cause of this destructive seismic event. The western Bozgush domain is relatively less deformed compared to the eastern domain. The change in the intensity and style of deformation in the eastern and western domains is a key aspect in understanding the rotational deformation history of the region, and assessing how Arabia-Eurasia convergence is accommodated in Northwest Iran.

1.2. Sampling

Paleomagnetic sampling was performed on Eocene volcanic rocks in the Qosha Dagh and Bozgush Mountains (Figure 2). A .kmz file with all sites is provided in Data Set S1. In total we sampled 127 sites and took nearly 600 samples. At least four samples were collected from most sites (Table 1). The Qosha Dagh profile consists of 11 sites of andesitic lavas along the road from Anzan toward the south. All sites are within unit Eb (Figure 2a), which includes olivine basalts, dacites and ignimbrites (Mahdavi & Amini Fazl, 1988). This unit was recently dated as late Eocene-Early Oligocene; 33.4–34.9 Ma, based on Ar-Ar geochronology of porphyritic andesite-basalts (Heidari et al., 2022).

The Bozgush West (BW) locality consists of several road sections along the western Bozgush Mountains, of which the longest one starts from the village of Varzeqan and ends at the village of Daman Jan and crosses the entire width of the Bozgush range (Figures 1 and 2b). BW includes 59 sites predominantly consisting of porphyritic andesites.

The Bozgush East transect consists of two localities, BE and BOZ. Sampling in the BE locality was performed along a transect of 3 km, following a road from Ardeha toward the south (Figure 2b). BE includes 21 sites, most of which are in unit Ev, which consists of pyroclastic rocks and lava flows (Amidi et al., 1978). The BOZ locality (BOZ 01–31) is a road section in the eastern Bozgush Mountains that starts from the village of Sorkheh Hesar and continues to the northeast. We have included BOZ32-37 in the BOZ locality since they are located within the same eastern Bozgush tectonic domain, east of the SYF, and paleomagnetically the directions are from the same distribution and significantly different from the BW locality (see statistics in Section 3.1). The BOZ locality therefore includes 39 sites within units Ev and Etv and consist mostly of trachyandesites and porphyritic andesites, with minor red beds and tuffs (see Table 1).

Age assignment is based on the available geologic maps (Amidi et al., 1978; Asadian et al., 1993; Behruzi & Amini Azar, 1992) for the Bozgush profiles. Most of the BOZ and BE sites consist of megaporphyritic andesite and trachyandesitic lava flows (Behruzi & Amini Azar, 1992). The BW sites comprise porphyritic andesites. Eocene ages for the succession are inferred based on the presence of Nummulites, which are common age diagnostic fossils in the Eocene volcaniclastic successions in Iran (Asiabanha et al., 2009).

2. Methods—Paleomagnetism

Samples were collected during two field campaigns in 2015 and 2017. Standard paleomagnetic core samples (25 mm diameter) were drilled using a gasoline-powered drilling machine and oriented by a magnetic compass. All orientations were corrected for a local declination at the time of sampling of ∼5° E (International Geomagnetic Reference Field [IGRF]). Additionally, orientations were measured using a sun compass whenever possible. In general, there was no significant difference between sun compass and magnetic compass measurements, but we used all available sun compass orientations. All cores were cut in the lab to standard sized specimens (22 mm) using a double-blade circular saw. Laboratory analyses were performed at the paleomagnetic laboratory Fort Hoofddijk (Utrecht University, The Netherlands).

Thermomagnetic runs were carried out on samples from different lithologies to identify possible magnetic carriers. Thermomagnetic runs were measured in air with a modified horizontal translation type Curie balance with a sensitivity of approximately 5×10^9 Am^2 (Mullender et al., 1993) using a cycling field, varying from 50–300 mT to 250–300 mT. Approximately 15–92 mg of powdered sample from representative lithologies was put into quartz

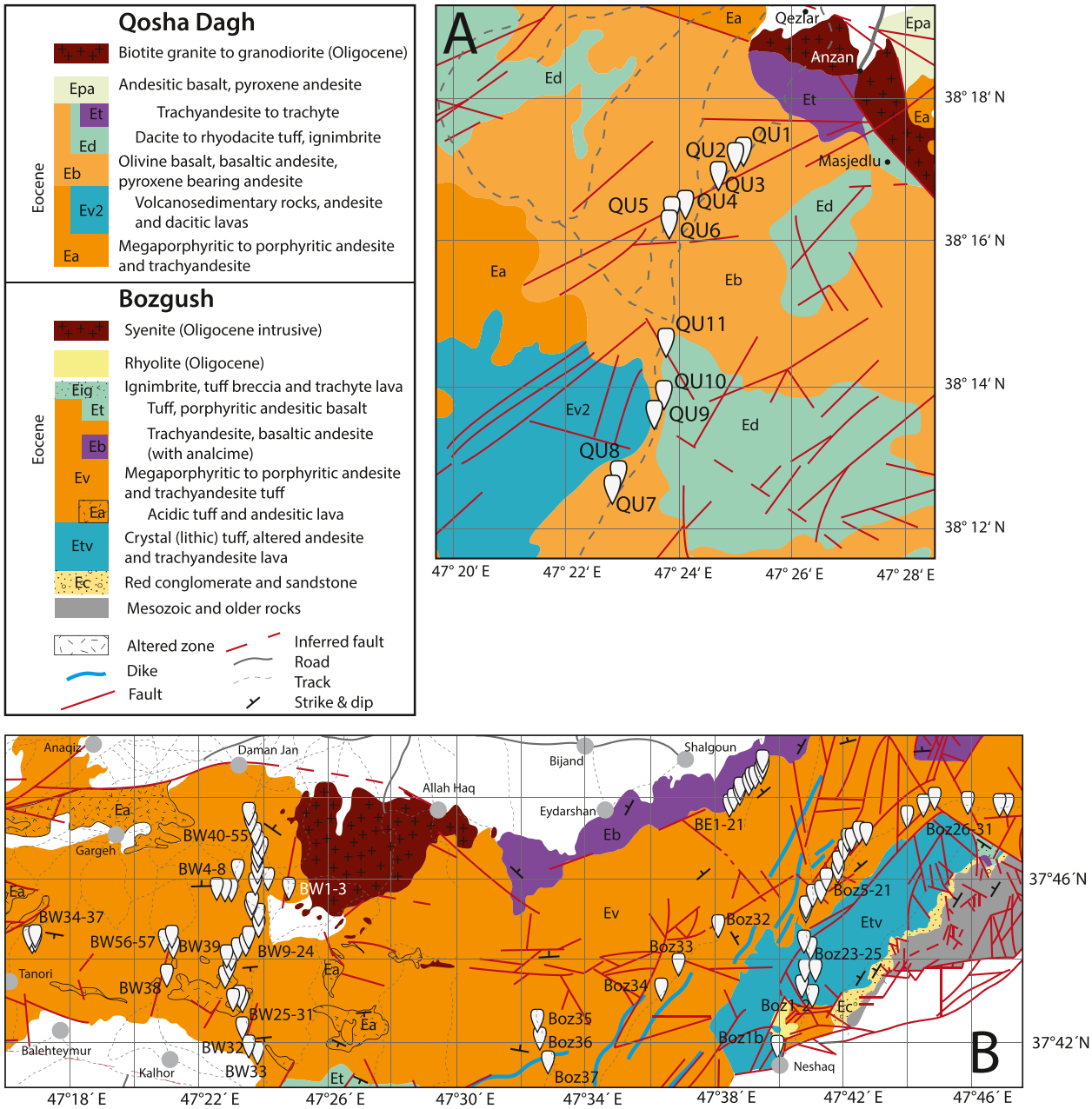

Figure 2. Detailed geological maps of the sampling areas (a) Qosha Dagh and (b) Bozgush, with locations of the sampled sites. The map of Qosha Dagh is modified after Mahdavi and Amini Fazl (1988), the Bozgush map is modified after Asadian et al. (1993) for the part west of 47°30′ E, and Behruzi and Amini Azar (1992) for the part east of 47°30′ E.

glass sample holders and was held in place by quartz wool; heating and cooling rates were 10°C/min. Stepwise thermomagnetic runs were carried out with intermittent cooling between successive heating steps.

Thermal demagnetization was performed in a magnetically shielded furnace with temperature increments from 20 to 80°C up to temperatures of 580°C, or 680°C if samples contained hematite. Alternating Field (AF) demagnetization was performed in steps of 5–10 mT using an in in-house built and robotized 2G DC-SQUID magnetometer (Mullender et al., 2016). Natural remanent magnetizations were measured on a 2G Enterprise horizontal cryogenic magnetometer, equipped with three DC SQUIDS (noise level 3×10^{-12} Am^2), after each demagnetization step. Samples generally show strong magnetizations, in some cases above the range of the magnetometer. These measurements are characterized by extremely high errors, and are removed from our interpretation.

Tectonics

10.1029/2023TC008139

Table 1
Locations and Paleomagnetic Data of All Sites per Locality

Means per site																		
Site	Latitude (°N)	Longitude (°E)	Samples taken	N_{45} (NOTC)	N (NOTC)	Dec (NOTC)	Inc (NOTC)	N_{45} (TC)	N (TC)	Dec (TC)	Inc (TC)	k	$\alpha 95$	#GC	Specimens demagnetized	Bedding strike	Dip	Lithology
Qosha Dagh																		
QU01	38.283957	47.418673	5	10	10	58.4	44.3	10	10	57.8	19.3	57.4	6.4	3	10	326	25	Andesitic lava
QU02	38.282799	47.416486	4	6	6	58.6	38.6	6	6	57.7	13.7	178.2	5.0		6	324	25	Andesitic lava
QU03	38.27853	47.411304	4	5	5	76.1	47.1	5	5	74.4	31.2	280.0	4.6		5	338	16	Andesitic lava
QU04	38.271504	47.401506	4	9	9	61.4	62.0	9	9	159.9	66.8	607.0	2.1		9	115	40	Andesitic lava
QU05	38.270164	47.397673	5	11	11	51.3	63.6	11	11	100.9	45.2	398.3	2.3		11	50	37	Andesitic lava
QU06	38.267525	47.396983	2	3	3	60.5	55.4	3	3	18.3	64.4	3,048.8	2.2		3	200	25	Andesitic lava
QU07	38.205841	47.380369	5	9	9	16.9	66.3	9	9	339.4	77.7	389.6	2.6		9	136	16	Andesitic lava
QU08	38.209115	47.381966	5	5	5	57.5	72.6	5	5	119.0	86.5	476.9	3.5		5	136	16	Andesitic lava
QU09	38.223127	47.392437	5	10	10	28.0	46.8	10	10	10.4	33.9	211.1	3.3		10	231	24	Andesitic lava
QU10	38.227659	47.395384	3	3	5	119.8	63.5	3	5	119.8	63.5	11.4	38.4		5	0	0	Andesitic lava
QU11	38.239641	47.396087	4	5	5	47.6	67.5	5	5	71.9	33.6	256.2	4.8	3	5	0	38	Andesitic lava
Bozgush West																		
BW01	37.7622992	47.3958179	11	4	4	54.2	72.3	4	4	49.1	47.5	74.0	10.8		6	315	25	Andesitic lava
BW02A	37.7610861	47.4031172	4	4	4	107.2	25.1	4	4	111.9	31.9	54.2	12.6		4	148	11	Andesitic lava
BW02B	37.7610861	47.4031172	4	2	4	15.3	58.1	3	4	22.4	50.7	8.5	45.3		4	315	25	Andesitic lava
BW03	37.7590825	47.4140155	4	4	4	71.4	21.4	4	4	72.8	32.1	216.1	6.3		4	148	11	Shoshonite
BW04	37.7648592	47.3867928	4	4	4	51.2	48.2	4	4	29.2	58.6	65.9	11.4	1	4	188	19	Andesitic lava
BW05	37.7604362	47.3855563	4	4	4	138.0	33.2	4	4	126.7	64.0	56.5	12.3		4	240	32	Andesitic lava
BW06	37.7588138	47.3839246	4	4	4	132.4	28.4	4	4	111.1	45.8	1,585.3	2.3		4	270	32	Tephriphonolite
BW07	37.7589803	47.3816249	4	4	4	35.9	−59.8	4	4	110.9	−71.6	19.7	21.3	2	4	270	32	Andesitic lava
BW08	37.75899	47.3763339	5	2	3	242.3	11.8	2	3	254.8	30.1				3	278	36	Andesitic lava
BW09	37.7542393	47.3959156	4	2	3	97.1	70.0	2	3	30.7	48.3				3	270	40	Andesitic lava
BW10	37.7513314	47.3951696	4	2	2	44.3	18.6	2	2	43.2	−14.8				3	270	45	Andesitic lava
BW11	37.7471336	47.3979131	4	2	2	250.9	−50.8	2	2	220.7	−23.7				3	270	45	Tephriphonolite
BW12	37.7413854	47.3970617	4	2	3	241.1	70.0	2	3	264.7	43.3				3	193	30	Andesitic lava
BW13	37.7413899	47.3961455	4	3	3	56.2	22.4	3	3	41.0	40.3	188.1	9.0		3	193	30	Andesitic lava
BW14	37.7382234	47.3920293	5	4	4	76.8	28.9	4	4	61.6	54.2	95.0	9.5	2	4	193	30	Andesitic lava
BW15	37.7379051	47.3928275	4	4	4	46.8	60.0	4	4	348.1	62.8	106.2	9.0		4	193	30	Andesitic lava
BW16	37.7352652	47.3896103	4	2	4	64.0	60.2	2	4	91.5	62.2				4	85	15	Andesitic lava
BW17	37.7334342	47.3910626	4	2	4	347.5	−27.4	2	4	348.2	−12.5				4	85	15	Basalt
BW18	37.7321847	47.3879393	4	4	4	91.6	15.6	4	4	95.5	13.4	54.5	12.6	3	4	85	15	Andesitic lava
BW19	37.731796	47.387947	4	2	4	104.1	−6.0	2	4	102.0	−10.7				4	85	15	Andesitic lava
BW20	37.7319197	47.3853564	4	3	3	18.9	60.9	3	3	39.1	73.5	57.9	16.4		4	85	15	Andesitic lava

Tectonics

10.1029/2023TC008139

Table 1
Continued

Means per site

Site	Latitude (°N)	Longitude (°E)	Samples taken	N_{45} (NOTC)	N (NOTC)	Dec (NOTC)	Inc (NOTC)	N_{45} (TC)	N (TC)	Dec (TC)	Inc (TC)	k	$\alpha 95$	#GC	Specimens demagnetized	Bedding strike	Dip	Lithology
BW21	37.7291723	47.3835348	5	5	5	62.3	25.6	5	5	69.9	30.5	35.6	13.0		5	85	15	Latite
BW22	37.7276699	47.3823185	4	4	4	31.1	21.3	4	4	36.0	33.0	70.8	11.0		4	85	15	Andesitic lava
BW23 — HT	37.725921	47.3817384	6	4	4	98.3	71.6	4	4	130.8	63.9	26.2	18.3		4	85	15	Andesitic lava
BW23 — MT	37.725921	47.3817384	6	4	4	274.8	−71.3	4	4	308.3	−64.3	22.5	19.8		4	85	15	Andesitic lava
BW24	37.7234817	47.3805091	4	5	5	63.2	41.8	5	5	77.2	45.7	112.2	7.3	1	5	85	15	Aplitic lava
BW25	37.7132958	47.3855632	4	4	4	11.1	16.7	4	4	13.1	31.0	72.7	10.9		4	85	15	Andesitic lava
BW26	37.7123964	47.3838256	4	3	3	32.5	−10.5	3	3	31.8	1.5	1,838.4	2.9		3	85	15	Andesitic lava
BW27	37.7105225	47.3895249	4	4	4	63.5	30.2	4	4	72.7	34.6	874.0	3.1	1	5	85	15	Tephriphonolite
BW28 — MT	37.7089615	47.3891399	4	4	4	238.3	−30.5	4	4	247.5	−36.2	72.4	10.9		4	85	15	Tephriphonolite
BW28 — HT	37.7089615	47.3891399	4	4	4	49.2	36.2	4	4	60.1	43.8	47.6	13.5		4	85	15	Tephriphonolite
BW29	37.7062172	47.3891528	4	4	4	38.0	16.4	4	4	42.3	27.0	301.8	5.3		4	85	15	Tephriphonolite
BW30	37.7057726	47.3893461	4	4	4	35.9	32.4	4	4	44.1	43.0	140.4	7.8		4	85	15	Shoshonite
BW31	37.7007005	47.3890743	4	4	4	12.5	12.5	4	4	14.2	26.8	167.9	7.1		4	85	15	Andesitic lava
BW32	37.6939792	47.3935368	4	4	4	20.8	22.2	4	4	24.7	35.5	179.1	6.9		5	85	15	Andesitic lava
BW33 — HT	37.6912392	47.3958704	5	5	5	6.7	17.9	5	5	8.3	32.5	19.5	17.8		5	85	15	Andesitic lava
BW33 — MT	37.6912392	47.3958704	5	3	3	196.1	−50.8	3	3	206.7	−64.3	113.8	11.6		5	85	15	Andesitic lava
BW34	37.7363829	47.279898	5	8	10	49.2	30.4	8	10	44.5	25.5	93.7	5.8		10	256	10	Andesitic lava
BW35	37.7369228	47.2818688	5	6	6	32.4	59.2	6	6	28.8	52.7	17.0	16.7		10	280	7	Andesitic lava
BW36	37.7383505	47.2815493	5	8	8	52.5	25.6	8	8	50.5	20.3	15.2	14.7		8	280	7	Andesitic lava
BW37	37.7385167	47.2803578	4	7	7	59.9	13.9	7	7	58.8	9.4	11.8	18.4		7	283	23	Andesitic lava
BW38	37.7231925	47.3491406	5	11	11	243.9	−30.3	11	11	236.9	−14.6	225.3	3.1		10	283	23	Andesitic lava
BW39	37.7344172	47.3526746	5	7	7	252.9	−55.8	7	7	249.5	−46.2	825.6	2.1		7	325	10	Andesitic lava
BW40 — HT	37.7625795	47.3965761	4	4	4	78.8	67.8	4	4	62.5	55.5	30.6	16.9		4	305	15	Andesitic lava

Tectonics
10.1029/2023TC008139

Table 1
Continued

Means per site

Site	Latitude (°N)	Longitude (°E)	Samples taken	N_{45} (NOTC)	N (NOTC)	Dec (NOTC)	Inc (NOTC)	N_{45} (TC)	N (TC)	Dec (TC)	Inc (TC)	k	$\alpha95$	#GC	Specimens demagnetized	Bedding strike	Dip	Lithology
BW40—MT	37.7625795	47.3965761	4	1	1	193.0	−56.3	1	1	198.7	−42.1				4	305	15	Andesitic lava
BW41	37.7643627	47.397319	5	4	4	322.8	45.0	4	4	335.2	38.8	89.6	9.8	2	4	305	15	Andesitic lava
BW42	37.7650527	47.3976808	4	4	4	343.2	62.2	4	4	359.2	51.3	14.5	25.0		4	305	15	Andesitic lava
BW43	37.76549	47.3979774	4	4	4	241.9	−61.0	4	4	233.8	−47.2	56.8	12.3	2	4	305	15	Andesitic lava
BW44	37.7676113	47.3979268	5	4	4	100.9	62.4	4	4	80.8	53.8	243.8	5.9		4	305	15	Felsic lava
BW45	37.7705302	47.3980268	4	4	4	357.8	74.6	4	4	15.5	61.2	32.4	16.4		4	305	15	Andesitic lava
BW46	37.7709733	47.3979305	5	5	5	57.0	76.5	5	5	45.8	62.0	91.6	8.0		5	305	15	Andesitic lava
BW47	37.7720894	47.3982089	5	5	5	88.8	82.2	5	5	53.1	69.4	110.3	7.3		5	305	15	Latite
BW48	37.7725093	47.3984123	4	4	4	115.6	81.2	4	4	63.3	71.5	311.2	5.2	1	4	305	15	Andesitic lava
BW49	37.7735554	47.398415	5	5	5	72.6	80.3	5	5	50.0	66.6	237.4	5.0	1	5	305	15	Latite
BW50	37.7744949	47.3977757	4	4	4	78.6	76.0	4	4	56.7	63.1	72.7	10.9		4	305	15	Andesitic lava
BW51	37.7764836	47.3977137	4	4	4	69.9	46.9	4	4	63.2	34.0	90.2	9.7		4	305	15	Andesitic lava
BW52	37.7787311	47.3957678	7	5	5	64.5	50.2	5	5	58.2	36.7	45.7	11.4		5	305	15	Phonotephrite
BW53	37.7810365	47.3944921	4	4	4	57.7	37.2	4	4	54.5	23.1	74.4	10.7		4	305	15	Andesitic lava
BW54	37.7843914	47.3928653	3	3	3	54.2	44.2	3	3	50.8	29.9	70.7	14.8		3	305	15	Andesitic lava
BW55	37.7878817	47.3927306	4	3	3	238.1	−31.8	3	3	235.5	−17.9	881.8	4.2	1	3	305	15	Andesitic lava
BW56	37.7359887	47.3510258	5	7	10	74.7	−36.9	6	10	78.2	−50.1	12.3	17.9		10	335	20	Andesitic lava
BW57	37.73758	47.3525797	5	10	10	276.8	−66.4	10	10	246.0	−62.4	189.6	3.5		10	276	15	Andesitic lava
Bozgush East																		
BE01	37.7924092	47.641318	8	4	4	69.6	7.2	4	4	62.8	16.6	41.7	14.4	1	4	230	33	Porphyritic trachyandesite
BE02	37.7933654	47.6420086	5	4	4	72.8	9.3	4	4	64.3	20.1	463.3	4.3		4	230	33	Gray fine-grained lava
BE03	37.793016	47.642515	4	4	4	91.6	12.8	4	4	80.1	32.6	33.3	16.2	1	4	230	33	Porphyritic lava
BE04	37.7931511	47.6424669	4	4	4	77.4	−1.3	4	4	74.2	13.4	357.4	4.9		4	230	33	Porphyritic lava
BE06	37.7973327	47.6454718	6	5	5	134.3	16.3	4	5	118.3	45.6	12.8	26.7		5	230	33	Gray tuffbreccia
BE07	37.7980878	47.6464388	5	5	5	133.2	1.4	5	5	131.8	34.1	41.4	12.0		5	230	33	Tuffaceous sediment
BE08	37.798775	47.6461727	5	4	4	124.0	14.1	4	4	117.7	45.4	96.3	9.4		3	230	33	Latite
BE09	37.7998806	47.6465372	5	5	5	98.4	26.9	5	5	77.8	47.9	275.2	4.6		5	230	33	Andesitic lava
BE10	37.8003237	47.6473616	5	4	4	102.6	23.0	4	4	85.6	46.6	309.7	5.2		4	230	33	Andesitic lava
BE11	37.8004699	47.6484968	6	4	4	112.0	21.4	4	4	98.3	49.0	118.2	8.5		4	230	33	Latite
BE12	37.8000742	47.6496115	4	2	4	106.5	−14.7	2	4	106.8	13.1				4	230	33	Andesitic lava
BE13	37.8001499	47.6503043	6	4	4	87.3	20.7	4	4	70.9	37.3	816.3	3.2	2	4	230	33	Shoshonite
BE14	37.8006434	47.6510096	5	4	4	63.2	44.3	4	4	30.7	42.5	186.6	6.7		4	230	33	Shoshonite

Tectonics
10.1029/2023TC008139

Table 1
Continued

Means per site

Site	Latitude (°N)	Longitude (°E)	Samples taken	N_{45} (NOTC)	N (NOTC)	Dec (NOTC)	Inc (NOTC)	N_{45} (TC)	N (TC)	Dec (TC)	Inc (TC)	k	$\alpha 95$	#GC	Specimens demagnetized	Bedding strike	Dip	Lithology
BE15	37.8015889	47.6528805	6	5	5	72.4	−7.1	5	5	72.7	5.9	153.5	6.2		5	230	33	Andesitic lava
BE16	37.8026058	47.6536099	6	4	6	81.4	0.4	4	6	76.9	16.8	58.3	12.1		6	230	33	Andesitic lava
BE17	37.8034219	47.6541226	5	5	5	109.0	19.5	5	5	95.6	46.1	111.8	7.3		5	230	33	Andesitic lava
BE18	37.8042876	47.6552396	6	4	4	108.6	27.7	4	4	89.5	53.3	108.7	8.9		4	230	33	Andesitic lava
BE19	37.8052393	47.6558268	6	4	4	106.1	22.6	4	4	90.1	47.7	176.0	6.9		4	230	33	Andesitic lava
BE20	37.8082323	47.6586059	6	4	4	87.8	19.5	4	4	72.1	36.5	251.1	5.8		4	230	33	Andesitic lava
BE21	37.8096537	47.6583996	6	4	4	270.6	8.3	4	4	269.5	−13.3	253.7	5.8		4	230	33	Andesitic lava
BOZ01	37.7179332	47.6804861	6	4	4	197.5	5.2	4	4	197.7	−9.1	121.9	8.4		4	90	15	Phonotephrite
BOZ01b	37.6936913	47.6662966	2	2	2	4.2	−9.4	2	2	8.2	16.9				2	30	60	Green tuffbreccia
BOZ02	37.7148356	47.6828158	4	4	4	249.4	6.1	4	4	248.6	0.7	728.3	3.4		4	90	15	Andesitic lava
BOZ03	37.78038	47.71419	4	4	4	246.6	−25.1	4	4	236.4	−29.2	202.2	6.5	1	4	230	20	Shoshonite
BOZ04	37.7795536	47.7130537	5	4	4	256.9	−22.4	4	4	247.7	−30.0	13.3	26.1		4	230	20	Baked contact
BOZ05	37.7804749	47.7097404	6	4	4	296.5	−23.0	4	4	290.9	−41.0	238.6	6.0		4	230	20	Shoshonite
BOZ06	37.7804523	47.7092919	5	4	4	291.6	−26.4	4	4	284.1	−43.4	21.2	20.4	1	4	230	20	Andesitic lava
BOZ07	37.7761433	47.7052496	4	4	4	305.0	−27.0	4	4	300.6	−46.1	66.7	11.3		4	230	20	Andesitic lava
BOZ08	37.7749859	47.7047681	4	4	4	276.6	−23.2	4	4	264.8	−39.8	62.1	11.8		4	230	25	Andesitic lava
BOZ09	37.7744501	47.7041918	4	4	4	309.0	−30.7	4	4	303.4	−55.0	20.2	20.9		4	230	25	Andesitic lava
BOZ10	37.7736912	47.7023317	4	4	4	292.8	−20.2	4	4	284.9	−41.7	124.1	8.3		4	230	25	Andesitic lava
BOZ11	37.7727402	47.700657	3	3	3	288.1	13.4	3	3	288.1	−13.4	155.5	9.9		3	225	30	Andesitic lava
BOZ12	37.7697582	47.699727	4	4	4	282.3	2.6	4	4	279.3	−22.4	243.1	5.9		4	225	30	Andesitic lava
BOZ13	37.7692175	47.6988584	4	4	4	278.1	−21.0	4	4	264.8	−43.1	241.4	5.9		4	225	30	Baked contact
BOZ14	37.7648059	47.6995428	4	4	4	251.5	−6.7	4	4	240.1	−36.1	291.2	5.4		4	200	40	Andesitic lava
BOZ15	37.7645331	47.6968816	4	4	4	277.1	−38.5	4	4	273.8	−68.5	13.8	25.6		4	190	30	Baked contact
BOZ16	37.7640262	47.6937835	4	4	4	279.0	−26.3	4	4	273.8	−61.0	282.6	5.5		4	195	35	Andesitic lava
BOZ17	37.7616321	47.6916348	4	4	4	307.0	−11.9	4	4	318.1	−47.8	13.6	25.9		3	195	40	Baked red bed
BOZ18	37.7570442	47.6898361	4	3	3	286.5	−65.8	3	3	320.0	−34.1	326.2	6.8		3	75	40	Andesitic lava
BOZ19	37.7554672	47.6854418	3	3	3	350.8	−57.8	3	3	348.3	−17.9	104.5	12.1		3	75	40	Vesicular lava
BOZ20	37.7503786	47.6808616	4	4	4	266.4	−16.5	4	4	274.7	−9.9	108.2	8.9		4	80	35	Andesitic lava
BOZ21	37.7481082	47.681142	6	4	4	86.9	34.9	4	4	108.5	22.0	709.1	3.5	1	4	80	40	Andesitic lava
BOZ22	37.7481082	47.681142	5	3	4	53.6	52.6	3	4	99.9	60.3	10.3	40.5		4	90	30	Yellow-green sandy tuff
BOZ23	37.7355349	47.6806023	4	3	3	297.1	−12.4	3	3	300.2	−5.9	226.0	8.2	2	4	100	20	Red tuffbreccia
BOZ23b	37.7321691	47.6826851	4	2	2	200.9	−5.5	2	2	201.4	−22.4				4	105	17	Green tuffbreccia
BOZ24	37.7250481	47.6799863	4	4	4	237.0	0.3	4	4	237.9	−8.9	12.1	27.6		4	95	15	Tuffbreccia
BOZ25	37.723193	47.6827741	4	2	4	103.7	16.9	2	4	107.5	12.8				4	90	15	Andesitic lava

Tectonics

10.1029/2023TC008139

Table 1
Continued

Means per site

Site	Latitude (°N)	Longitude (°E)	Samples taken	N_{45} (NOTC)	N (NOTC)	Dec (NOTC)	Inc (NOTC)	N_{45} (TC)	N (TC)	Dec (TC)	Inc (TC)	k	$\alpha 95$	#GC	Specimens demagnetized	Bedding strike	Dip	Lithology
BOZ26	37.7874466	47.7331923	4	7	7	291.8	−57.7	7	7	276.0	−76.8	373.4	3.1	1	4	213	20	Andesitic lava
BOZ27	37.7905702	47.7413486	4	5	5	312.4	−17.2	5	5	314.8	−36.6	97.3	7.8	1	8	210	20	Andesitic lava
BOZ28	37.79433	47.7476554	4	7	7	71.2	1.4	7	7	74.1	−27.1	141.9	5.1		11	319	31	Andesitic lava
BOZ29	37.7920238	47.7646808	4	6	6	99.2	43.7	6	6	95.9	17.2	639.3	2.7		6	356	27	Andesitic lava
BOZ30	37.7916174	47.7810952	4	4	4	123.7	−14.2	4	4	143.6	−41.5	19.4	21.4		4	350	44	Andesitic lava
BOZ31	37.7917321	47.7840659	3	2	2	71.2	25.6	2	2	65.6	1.3				2	295	33	Andesitic lava
BOZ32	37.7417091	47.6353997	5	5	5	249.8	−14.2	5	5	250.9	−28.9	40.1	12.2		5	149	15	Andesitic lava
BOZ33	37.7265657	47.6136073	4	5	5	275.3	−25.5	5	5	281.1	−37.2	346.0	4.1		5	149	15	Andesitic lava
BOZ34	37.716125	47.6050822	5	7	7	271.9	−7.1	7	7	273.9	−19.6	25.3	12.2	1	9	149	15	Andesitic lava
BOZ35	37.7034743	47.5420124	4	6	7	262.1	43.1	6	7	250.5	37.0	11.2	21.0		7	100	15	Andesitic lava
BOZ36	37.6971236	47.5425103	4	8	8	240.5	2.4	8	8	240.9	−7.2	443.4	2.6		8	100	15	Andesitic lava
BOZ37	37.6870016	47.5466797	4	8	8	223.1	12.9	8	8	222.1	0.3	508.2	2.5		8	100	15	Andesitic lava

Note. Samples taken is the number of cores that were drilled at each site. N_{45} represents the number of specimens remaining after the 45° cut-off, N is the total number of specimens interpreted. Sites with $N_{45} < 3$ are marked in yellow. NOTC is in geographic coordinates (before bedding correction), TC is in tectonic coordinates (after applying bedding correction). k, α_{95} are the Fisherian precision parameter and cone of confidence, respectively. Sites that do not pass the cut-off criterion of $k > 50$ are marked in red. $\#_{GC}$ is the number of great-circle interpretations that went into the calculated directions. Specimens demagnetized is the total number of specimens that were demagnetized, which in rare cases differs from N, if specimens were present that did not yield interpretable directions. Bedding orientations for the Qosha Dagh sites are in gray, as we do not consider these to be an accurate representation of the bedding (see text for explanation).

Statistical analysis and interpretation were done using the on-line, platform independent portal paleomagnetism.org (Koymans et al., 2020). Demagnetization diagrams are plotted as orthogonal vector diagrams (Zijderveld, 1967) and results were calculated using principal component analysis (Kirschvink, 1980). Interpretation of demagnetization diagrams was performed by determining a characteristic remanent magnetization (ChRM) for components decaying toward the origin. We determined great circles if we found no clear ChRM decaying toward the origin because of a pervasive (low temperature or low coercive) overprint causing overlapping blocking temperatures or coercivity. Lines (ChRM, denoted as "set points") and planes (great circles) were determined following an eigenvector approach (Kirschvink, 1980). If we have both set points and great circles in a site, we use the method of McFadden and McElhinny (1988) to determine great circle solutions. We applied a 45° cut-off to the virtual geomagnetic pole (VGP) distribution of a set of directions (following Deenen et al., 2011). Mean directions were determined using standard Fisher statistics, whereas directional statistics were derived from the corresponding VGP distribution (Deenen et al., 2011), and errors in declination (ΔD_x) and inclination (ΔI_x) were calculated from the cone of confidence (A95) of the mean VGP following Butler (1992). We applied the reliability criteria of Deenen et al. (2011) by determining A95 of the VGP distribution, and calculate the N-dependent values of $A95_{min}$ and $A95_{max}$ (recalculated by Deenen et al., 2014).

3. Results

Thermomagnetic runs are shown in Figure 3. Most samples show a rapid decrease in magnetization upon heating, with generally irreversible behavior. Samples BW05, BW13, BW55 are exceptions, and show overall reversible behavior. Some samples (Boz08, BW52, BE04, BE04a) show a slight increase in magnetization around 150°C, possibly caused by oxidation of magnetite (van Velzen and Zijderveld, 1995). Nearly all samples show Curie temperatures around 580°C, pointing to (Ti-poor) magnetite as the main magnetic carrier. Several samples contain (additional) hematite, as indicated by maximum unblocking temperatures of around 680°C.

All demagnetization diagrams with interpretations for each specimen are given in Data Set S2 (.col files that can be opened in the interpretation portal of paleomagnetism.org; Koymans et al., 2020). Samples generally show small low-temperature or -coercivity components, and mostly linearly decay to the origin of Zijderveld diagrams up to temperatures of 580°C (Figure 4), or 80 mT. Some samples show no decay upon AF demagnetization, and thermal demagnetization up to temperatures of 680°C, corresponding to the presence of hematite. Characteristic remanent magnetizations (ChRMs) are generally interpreted above 25–35 mT or 300–450°C in case of magnetite, and above 500–580°C in case of hematite. Some sites, such as BW23 (Figure 4k), show two components (medium temperature [MT] and high temperature [HT]) that are antipodal (Figure 4l). Figure 4m shows a case where we have used great-circle analysis.

Means per site, grouped by locality, are shown in Table 1 and Figure 5. All averages per locality are supplied in Data Set S3 (.pub files that can be opened in the statistics and geography portals of paleomagnetism.org). Following Biggin et al. (2008), we use $k > 50$ as a criterion for the site recording a spot reading of Earth's magnetic field which leads to the elimination of 29 sites in total. All remaining sites with $N \geq 3$ are included in the calculation of the means per locality (Table 2) after converting all directions to normal polarity and taking a 45° cut-off (Figure 5). The spread in site means for each locality is relatively large, both before and after bedding correction, but conforms to recording secular variation ($A95_{min} < A95 < A95_{max}$; Deenen et al., 2011). Only the QU sites after bedding correction (TC) do not fall within this criterion, which is further discussed below.

3.1. Fold, Reversal and Common True Mean Direction Tests

Fold tests in our study are predominantly inconclusive or negative mainly because of small differences in bedding tilt, and difficulty in determining bedding in the volcanic successions that we have sampled (Figures 6a–6d).

Particularly the bedding planes of the QU sites could not be determined well, and are an estimate at best. Clustering of directions for the QU sites worsens when applying a bedding correction (Figure 6a), and this locality thus has a negative fold test (Tauxe & Watson, 1994). Such a distinctly negative fold test can be explained through several mechanisms. It can mean that samples were remagnetized and acquired a magnetization after folding, the sampled volcanic rocks were deposited on an initial slope, or bedding corrections were not correct. Indeed, determining bedding corrections in this area is uncertain due to the outcrop conditions and the variation in lithology. We consider remagnetization unlikely, due to the scatter in directions indicative of recording paleosecular variation, and the large declinations. If the QU sites were remagnetized after tilting, we might expect a

10.1029/2023TC008139

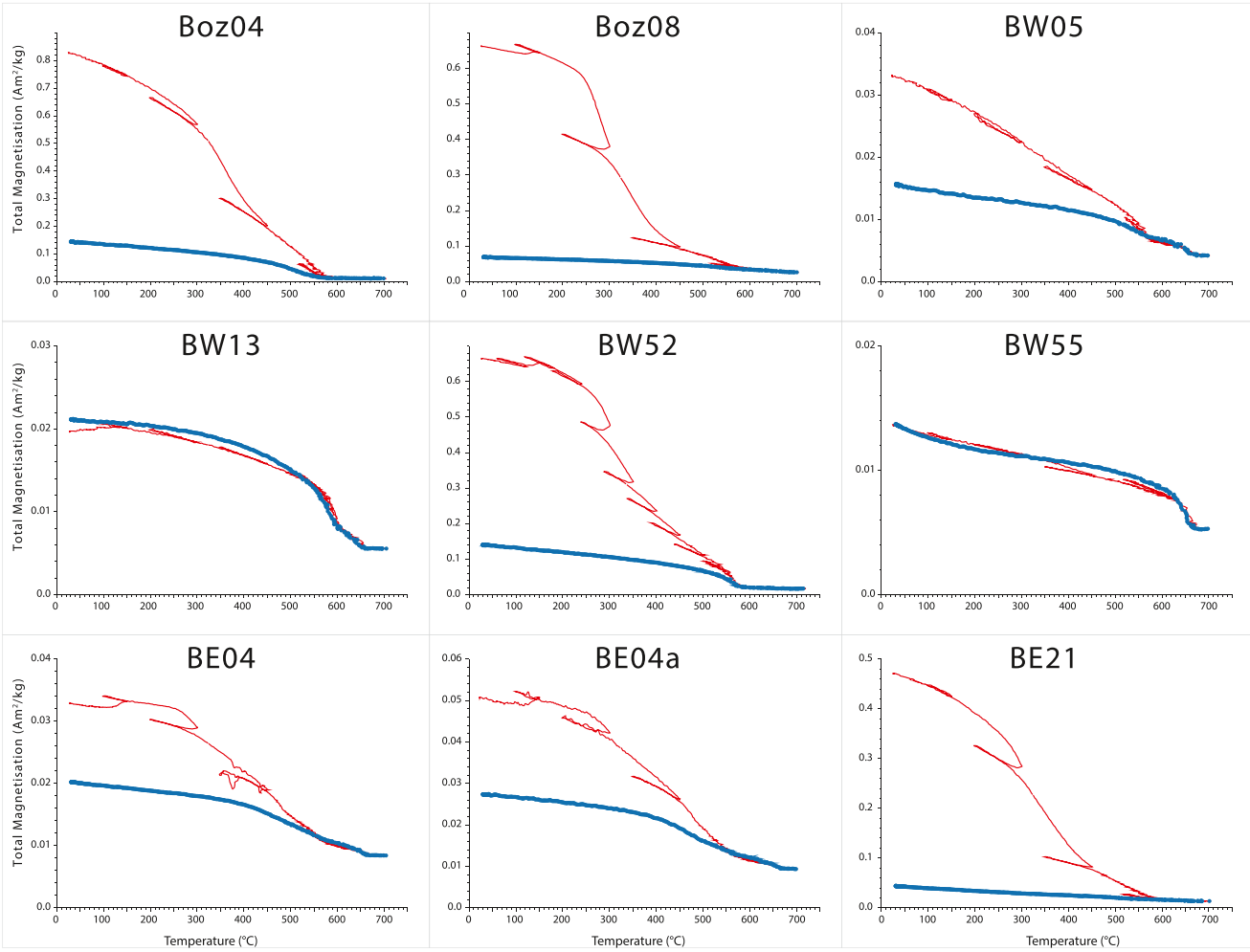

Figure 3. Curie balance thermomagnetic curves of representative samples. The heating/cooling cycles are represented by the red lines, the final cooling is indicated by the blue line.

better clustering of directions, unless remagnetization was acquired over a very long time span. The observed magnetizations may have been acquired after tilting but were clearly acquired prior to a significant amount of vertical axis rotation, as indicated by the large declinations (implying large rotations). Moreover, the recorded declinations are nearly identical in magnitude to those of the BW locality. Inclination data for the Qosha Dagh samples agree very well with the expected inclination for northwest Iran in the Eocene (Torsvik et al., 2012), indicating that possibly no tectonic correction is needed for this area. Heidari et al. (2022) presented a geological cross-section located at a distance of around 9 km from our sampled sites, in which they show that the Eocene volcanic unit is mostly flat lying. However, this is in contrast with a geological cross-section on the Ahar geologic map (Mahdavi & Amini Fazl, 1988), which is located at an equal distance from our sampled sites. Without further detailed mapping, we cannot conclusively determine whether Qosha Dagh sites represent a post-tilting remagnetization, or a primary magnetization of a flat lying unit. Either way, declinations before and after bedding correction are indistinguishable within error.

The BW sites show a convincingly positive fold test (Figure 6b), with maximum clustering including 100% [70, 150%] of unfolding.

The BE sites show an inconclusive fold test (Figure 6c; maximum clustering includes both 0% and 100% unfolding), due to the fact that all samples have similar bedding, thus there is no change in clustering of directions after bedding correction.

10.1029/2023TC008139

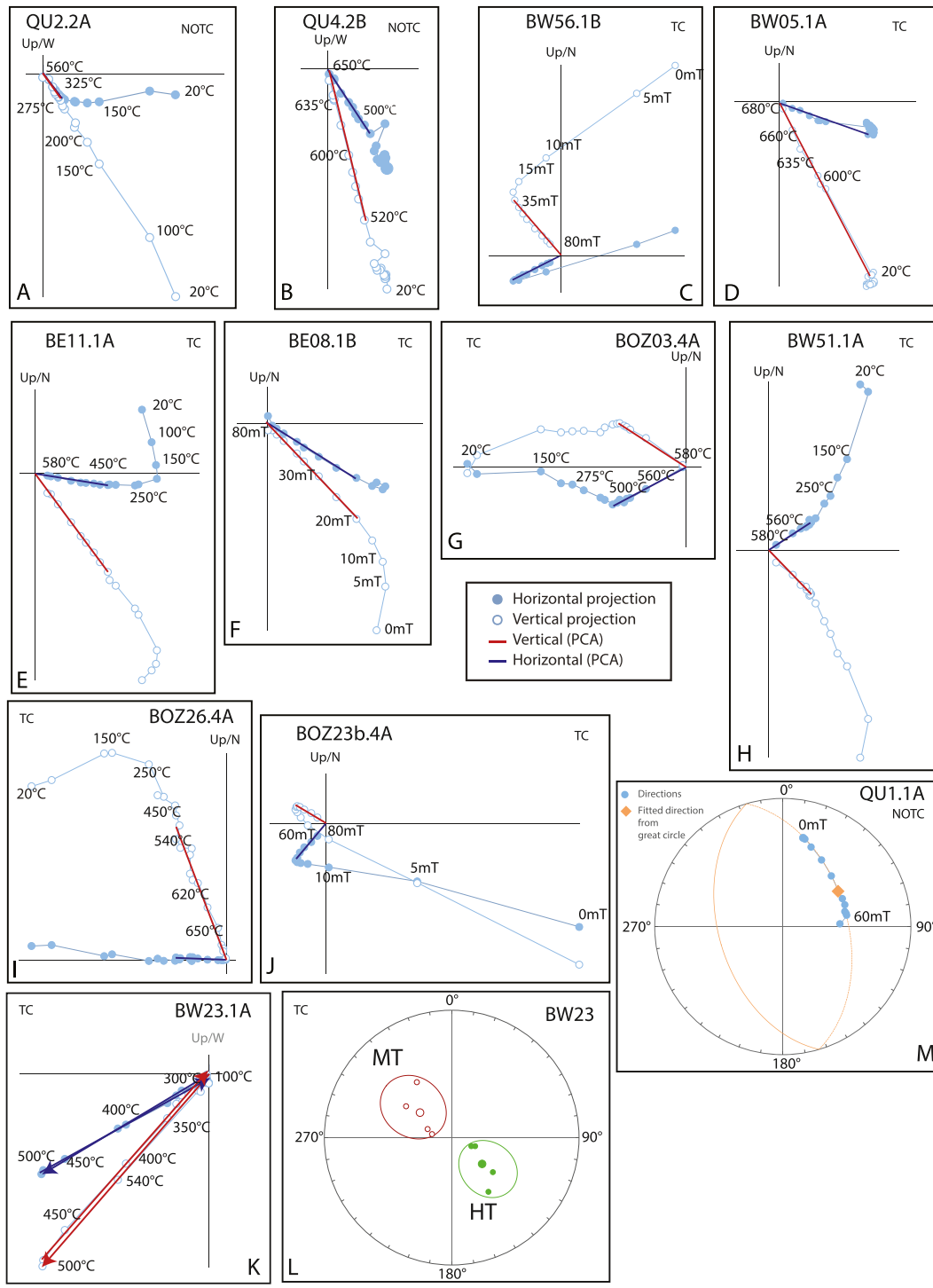

Figure 4. (a–k) Examples of representative Zijderveld diagrams with interpreted characteristic remanent magnetization (ChRM) directions projected on the vertical (horizontal) plane indicated by red (blue) lines. NOTC (TC) indicates geographic (tectonic) coordinates. (l) Equal area plot of average directions of samples of site BW23 with two antipodal components (MT, medium temperature; HT, high temperature). (m) Example of a great-circle interpretation.

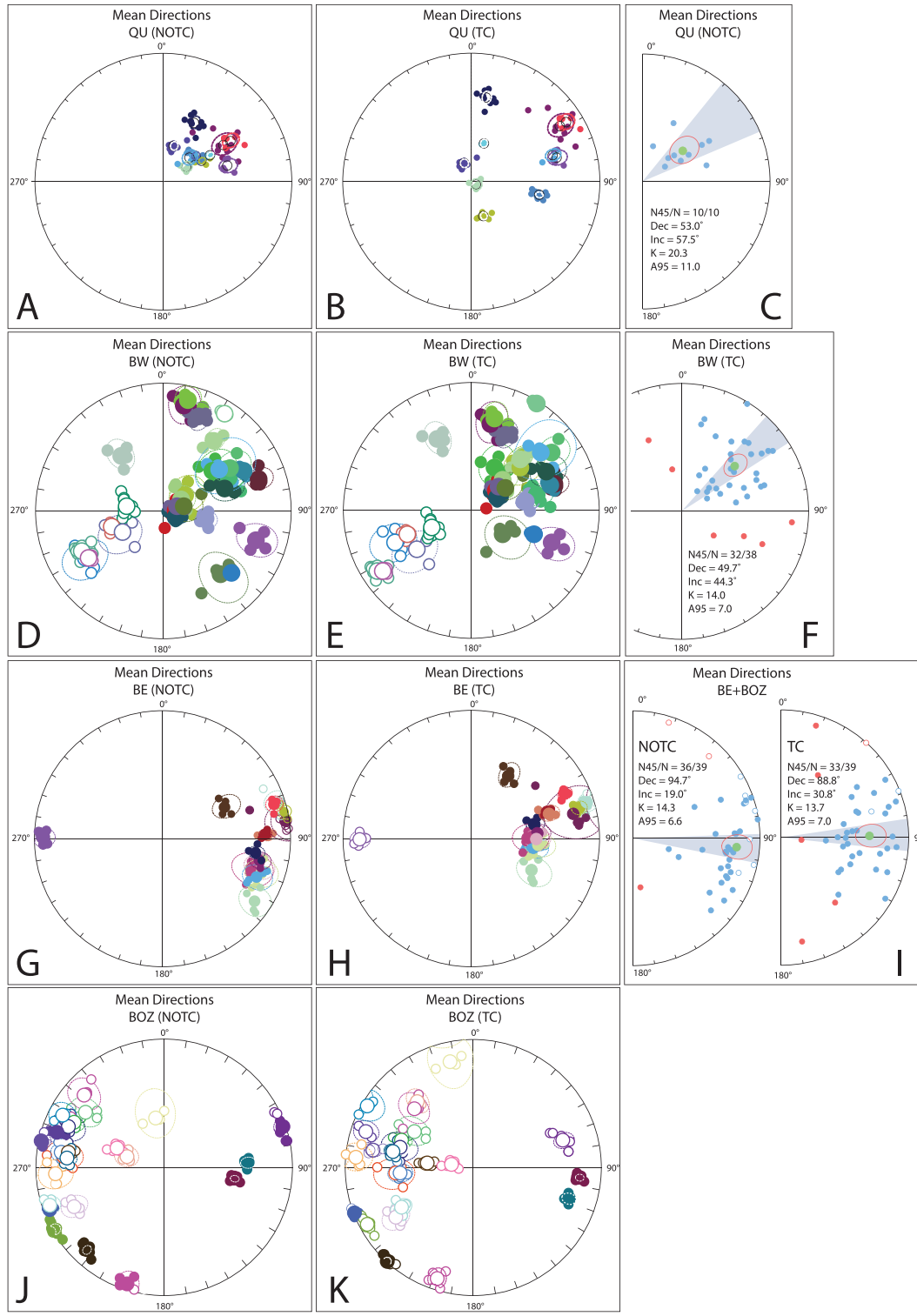

Figure 5. Equal area projections of site means ($k > 50$, $N_{45} \geq 3$) per locality in geographic (NOTC) and tectonic (TC) coordinates, and averages for the different localities.

Table 2
Means of Paleomagnetic Directions per Locality and per Block, Based on Sites With $N \geq 3$ and $k > 50$

	NOTC											TC										
Means per block	N_{45}/N	Dec	ΔD_x	Inc	ΔI_x	k	A95	K	A95	$A95_{min}$	$A95_{max}$	N_{45}/N	Dec	ΔD_x	Inc	ΔI_x	k	A95	K	A95	$A95_{min}$	$A95_{max}$
QU	10/10	53.0	14.0	57.5	10.2	29.9	9.0	20.3	11.0	4.8	19.2	6/10	55.6	32.4	38.1	42.7	6.9	27.6	6.0	29.9	5.9	26.5
BW	32/38	51.7	10.2	42.7	12.1	8.6	9.2	8.6	9.2	3.0	9.2	32/38	49.7	7.8	44.3	8.9	13.5	7.2	14.0	7.0	3.0	9.2
BE	15/15	93.1	9.2	16.2	17.2	13.9	10.6	18.6	9.1	4.1	14.9	14/15	82.5	8.9	35.1	12.7	16.6	10.0	23.3	8.4	4.2	15.6
BOZ	21/24	96.0	9.8	21.1	17.3	9.0	11.2	12.0	9.6	3.6	12.1	20/24	95.6	11.3	28.1	18.2	8.0	12.3	9.9	10.9	3.6	12.4
BE + BOZ	36/39	94.7	6.7	19.0	12.1	10.7	7.7	14.3	6.6	2.9	8.6	33/39	88.8	7.3	30.8	11.3	10.3	8.2	13.7	7.0	3.0	9.1
QU NOTC + BW TC	40/48	54.9	8.2	47.6	8.5	11.2	7.1	10.9	7.2	2.7	8.0											

Note. NOTC is in geographic coordinates (before bedding correction), TC is in tectonic coordinates (after applying bedding correction). The A95 value marked in red does not satisfy the $A95_{min} < A95 < A95_{max}$ criterion of Deenen et al. (2011).

The BOZ sites show a negative fold test, but with a very large uncertainty, with maximum clustering between −23% and 68% of unfolding (Figure 6d), rendering the fold test inconclusive. The fold test for the BOZ sites is not as distinctly negative as that of the QU sites, and we hypothesize that the difficulty in obtaining bedding for the volcanic rocks in the BOZ locality is the reason for this negative fold test. In any case, similar to the QU sites, the TC and NOTC results are indistinguishable within error. Furthermore, the observed magnetizations were clearly acquired prior to significant vertical axis rotations, as indicated by the large declinations.

3.2. Grouping of Directions

The directions from sites QU and BW share a common true mean direction (CTMD; Figure 6e), which means that they can be considered as deriving from the same population. This is also the case for sites BOZ and BE (Figure 6f). As locality QU has only normal polarities, and shares a CTMD with BW, we combined these sites for a reversal test (Figure 6g) which is positive. The BOZ sites are predominantly of reversed polarity (22 sites), with only two sites with a normal polarity. Conversely, the BE sites are predominantly of normal polarity (14 sites), with only one site with a reversed polarity. In order to perform reversal tests that are not biased by a low number of sites with one polarity and average out secular variation, and as BOZ and BE share a CTMD, we have added these sites together to perform a reversal test, which is positive (Figures 6g and 6h).

3.3. Rotations

The expected declinations for the Eocene in the sample region based on the Eurasia apparent polar wander path are around 11°, while inclinations are around 50° (Torsvik et al., 2012). The QU and BW sites show similar declinations of around 50° (Figures 5a–5f; Table 2), and inclinations of 57.5° ± 10.2 (QU; NOTC) and 44.3° ± 8.9 (BW; TC), respectively. Sites in the eastern domain of the Bozgush mountains show much larger declinations, of more than 90° (Figures 5g–5k; Table 2), and lower inclinations. Together, the mean of BOZ and BE includes 36 sites, and is Dec = 94.7° ± 6.7, Inc = 19.0° ± 12.1 (NOTC), or 33 sites with Dec = 88.8° ± 7.3, Inc = 30.8° ± 11.3 (TC) (see Figure 5i). A95 values satisfy the criterion of Deenen et al. (2011) $A95_{min} < A95 < A95_{max}$, which means that the distribution of our obtained paleomagnetic directions averages out paleosecular variation and provides a good representation of the geomagnetic field. The obtained declinations can be explained by differential vertical axis rotations, which can be calculated by comparing the obtained declinations with the expected declinations for the Eurasian plate in northwest Iran. This means that QU and BW sites experienced a post-magnetization clockwise vertical axis rotation of around 40°, while the BOZ and BE sites experienced a clockwise rotation of around 80°.

Many of our sampled sites, particularly in the BOZ and BE sites, show inclinations that are much lower than expected. Inclinations become somewhat steeper after bedding correction but are still almost 10° lower than the expected 50° for the Eocene (Torsvik et al., 2012). Shallow inclinations in volcanic rocks are a problem that has previously been reported from the region (Rezaeian et al., 2020; van der Boon et al., 2017) and beyond (Cogné et al., 1999; Si & Van der Voo, 2001; Westphal, 1993). But also Ballato et al. (2016) report too low inclinations

10.1029/2023TC008139

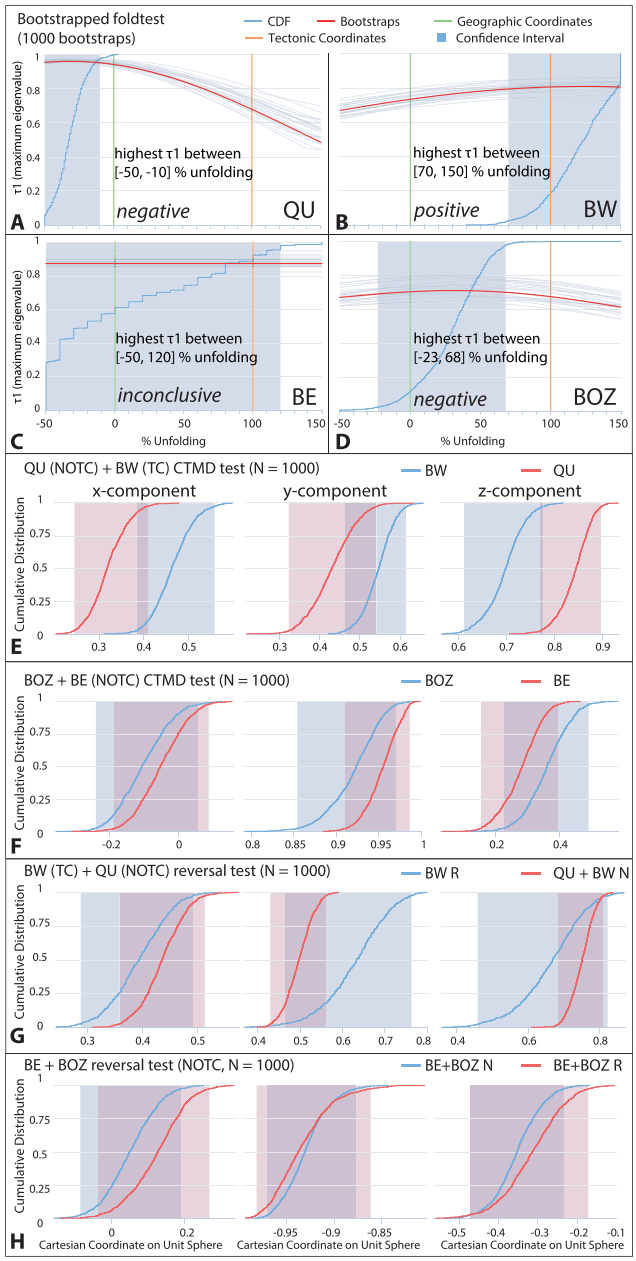

Figure 6. (a–d) Bootstrapped fold tests (Tauxe & Watson, 1994) for each locality. (e, f) Common true mean direction (CTMD) tests (Tauxe et al., 2010) for localities QU + BW and BE + BOZ. (g, h) Reversal tests for localities BW and BE + BOZ.

for Miocene sedimentary rocks in the Mianeh basin. It is unclear why these shallow inclinations are not observed in the Qosha Dagh region, as the inclinations of the QU and BW sites are in relatively good agreement with the expected values for the Eocene. We tentatively suggest that the explanation for this discrepancy could lie in the difficulties we had in obtaining accurate bedding corrections for the volcanic units.

4. Discussion

4.1. Structural Constraints and Timing

All sampled localities in our study have experienced significant vertical-axis clockwise (CW) rotation after the Eocene. The Qosha Dagh and western Bozgush domains show similar rotations of ∼40° clockwise, which can be explained either by a regional rotation of a block that consists of both localities, or by equal amounts of rotation related to right-lateral strike-slip movement along the Qosha Dagh and North and South Bozgush faults. We note however that commonly, right-lateral strike-slip movement is associated with counter-clockwise rotations (e.g., Mattei et al., 2020). We cannot currently distinguish between these two different models based on our paleomagnetic data set. However, we hypothesize that a regional rotation is the simplest model, as the QU and BW sites share a CTMD, and this model does not contradict the fact that right-lateral strike-slip faults are commonly associated with counter-clockwise vertical axis rotations.

Copley and Jackson (2006) hypothesized that right-lateral faults further to the northwest (Çaldıran fault, GSKF; Figure 1) have accommodated counter-clockwise rotations of crustal blocks in NW Iran. Our paleomagnetic data shows that there is no evidence for counter-clockwise rotations in the Qosha Dagh and Bozgush region, and the region instead shows evidence of clockwise rotations. It thus remains unclear whether the regional rotation is related to the activity of the right-lateral strike slip faults. The clockwise regional rotations that we observe could be accommodated by sinistral movement along the Aras and Lahijan faults (e.g., Rezaeian et al., 2020).

The eastern Bozgush domain has rotated much more; around 80° CW. This additional ∼40° CW rotation is likely related to the additional NNE-SSW striking faults that are only present in this domain (Figure 1b) (Faridi et al., 2017). If we discard the BOZ results because of the negative fold test due to possible remagnetization, we would end up with a rotation of around 70° CW for the Eastern Bozgush domain (instead of 80°), still considerably more than the western Bozgush domain. This would yield an additional rotation of 30° CW (instead of 40°), so remagnetization would change the numbers in our scenario below, but not the scenario itself.

The NNE-SSW striking faults are domino-style sinistral faults, which is consistent with the theoretical framework of Nur et al. (1986) in which crustal blocks in between strike-slip faults rotate like dominoes. In the case of the eastern Bozgush, this crustal block exhibits domino-style sinistral faults that accommodate clockwise rotation. Nur et al. (1986) reported that the amount of block rotation that a single set of faults can undergo is between 20 and 40°, with a maximum of 45°. If rotations are larger, a new set of faults will develop. Our additional 40° of rotation on top of the regional rotation of 40° fits well with these values and we hypothesize that the NNE-SSW fault system in the eastern Bozgush domain developed because the intersection between several crustal blocks prevented propagation of the large right-lateral strike-slip faults. Again, the role of the large, right-lateral faults in causing clockwise vertical axis rotations remains elusive. We suggest that paleomagnetic data can be well explained by a regional rotation

affecting the Qosha Dagh and entire Bozgush Mountains, and one domino-style set of faults affecting only the eastern Bozgush domain.

While there have been many studies on the large, right-lateral strike slip faults in NW Iran, it is unclear when these large faults initially formed. Copley and Jackson (2006) estimate the onset of fault displacement based on restoration of strike-slip motion indicators. They estimate that the GSKF may have initiated at 6.5 Ma, that is, during the late Miocene. Other authors estimate slightly younger ages of ~4 Ma (Pliocene; Mesbahi et al., 2016 and references therein) for the Tabriz fault. Gholami et al. (2021) performed thermochronology on the Bozgush mountains, and find evidence that first exhumation in the Bozgush Mountains began during the late Oligocene to early Miocene (25–19 Ma), but it presently remains unclear whether this exhumation was connected to strike-slip faulting.

Faridi et al. (2017) indicate that the sinistral NNE-SSW striking faults are conjugate to the larger dextral faults, and both fault sets are active at the present day. The NNE-SSW set of sinistral faults, however, shows much less offset, and we consider it thus likely that these faults have not been active for the same length of time. Faridi et al. (2017) note mostly a Holocene age for the left-lateral strike-slip faults.

4.2. Tectonic Model for the Qosha Dagh and Bozgush Mountains

To evaluate the tectonic deformation of the area, we provide a scenario that can explain the observed paleomagnetic data (Figure 7). The Bozgush Mountains consist mostly of a single unit of Eocene volcanic rocks (Amidi et al., 1978), which were formed during a volcanic phase prior to the Arabia-Eurasia collision. These volcanic rocks formed in a block that is likely initially curved (Figure 7a). Subsequently, the region experienced a clockwise rotation of around 40°, which affected a block that contained at least the Qosha Dagh and Bozgush areas. The second phase of rotation that is required to explain our paleomagnetic results is the domino-style faulting that affected only the eastern Bozgush domain. This scenario fits with the Benaravan fault as a restraining bend of the South Bozgush fault.

We consider that rotation in the region took place in two phases, due to the difference in rotations between the eastern and western Bozgush limbs. However, we note that these phases were not necessarily separated in time, as both fault systems are presently active (Faridi et al., 2017), and deformation could have happened progressively. We emphasize that our model is a preliminary one, and more detailed structural and paleomagnetic studies throughout Northwest Iran are required to elucidate the extent, timing and sense of block rotations throughout this region for a full tectonic reconstruction.

4.3. Shortening

Rotations in the overriding plate can take up shortening, as shown in the reconstruction for the Talesh-Alborz orocline by van der Boon et al. (2018). Because of a lack of further paleomagnetic constraints in NW Iran, we cannot estimate the amount of shortening taken up by the 40° regional rotation based on our current data. However, we can estimate the amount of shortening taken up by the domino-style faulting and additional 40° rotation in the eastern Bozgush domain.

The domino-style model leads to gaps or overlaps at the end of the rotating blocks, depending on how this space problem is accommodated (an overview is presented by Zuza & Yin, 2016), which leads to different estimates for shortening. The least shortening occurs when all sides of the blocks are preserved (L1 > L2 in Figures 7a–7c). This leads to a shortening of 5%. This is the scenario of Luyendyk et al. (1980), and can lead to the formation of basins at the ends of the rotated blocks.

Measuring the blocks following the method of Garfunkel and Ron (1985), in which one side of the blocks is preserved (L1>L3; Figure 7c) leads to shortening as high as 21%. Most shortening occurs when both sides of the blocks (Onderdonk, 2005) are not preserved. This leads to 39% shortening (L1>L4; Figure 7c).

While it is difficult to distinguish between the different models, the geologic map of Sarab (Behruzi & Amini Azar, 1992) seems to show a stepwise offset at the southern edge of the domino blocks, indicating that the edges of blocks are preserved at least along the southern side of the Bozgush Mountains. Here, the blocks border Miocene sedimentary rocks. Thus, the Onderdonk (2005) model, which does not preserve the edges of the block and stepwise offsets (see also Zuza & Yin, 2016), is likely not a good representation for the eastern Bozgush

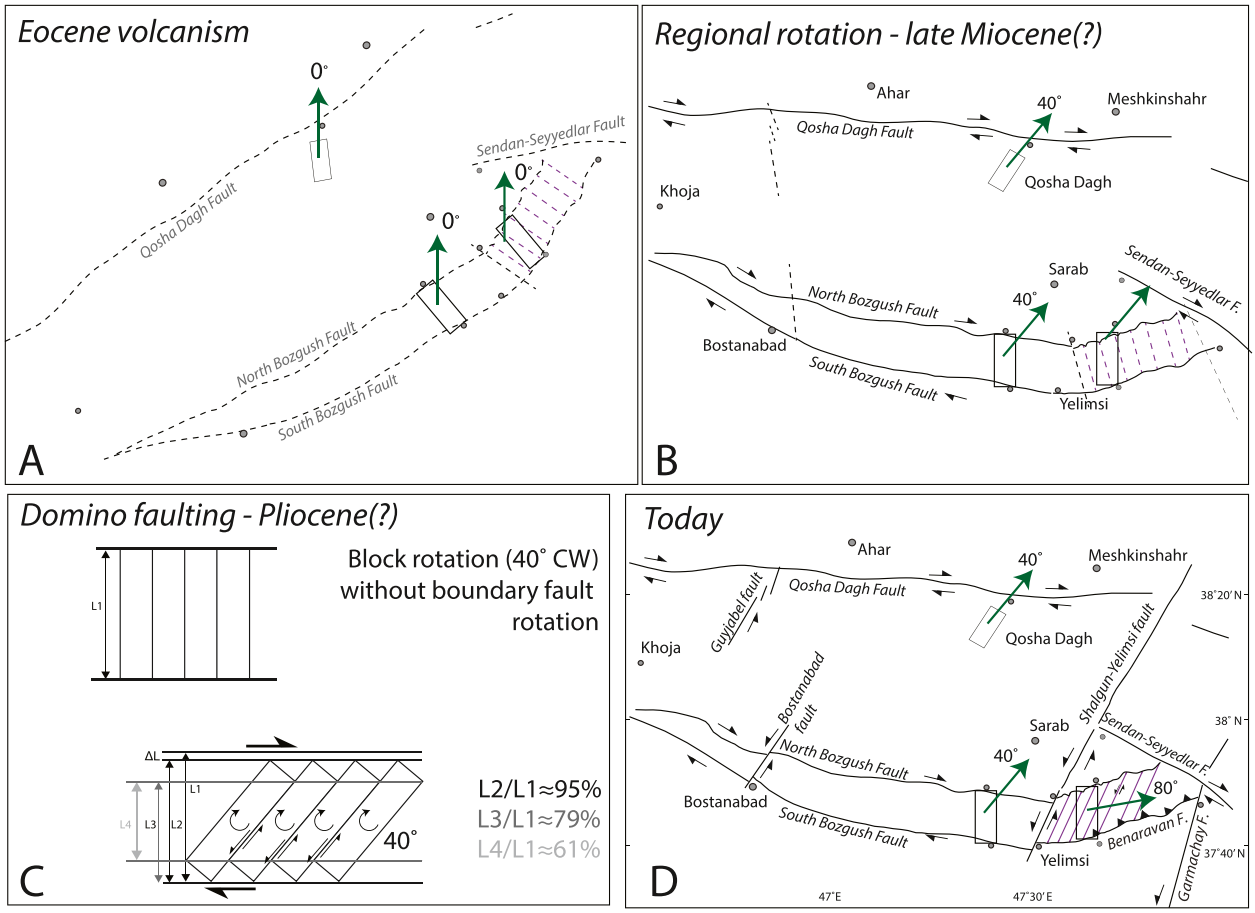

Figure 7. Graphical representation of the tectonic scenario that can explain the paleomagnetic data, with estimates of the accommodated shortening. Faults are dotted in (a) to indicate that these faults were not yet active during the Eocene, but are shown here to indicate the orientation of the Bozgush and Qosha Dagh Mountains.

domain. On the northern side, things are less clear, as the northern edge of the eastern Bozgush domain is covered by Quaternary sediments, and a stepwise offset is not easily distinguished.

Shortening is then estimated between 5% and 21% for scenario L2/L1—L3/L1 (see Figure 7c). Using an estimate of block length (measured using maps and Google Earth) of ~17 km, and a distance between the North and South Bozgush fault of around 13 km leads to a shortening estimate of 24%, which corresponds to partial preservation of the blocks. These percentages likely correspond to around 4 km of shortening that is taken up by the eastern Bozgush domain for block lengths of 17 km. Fault offsets based on the Sarab geologic map are between 1 and 3 km, which fits well with our scenario. It is noteworthy that the distance between bounding faults on the northern and southern sides of the Bozgush Mountains is approximately equal on the eastern and western sides of the SYF today. Given the north-south shortening, the initial distance between the northern and southern boundary faults must have been comparatively larger in the Eastern Bozgush domain in the past. Over time, as the blocks within the larger Eastern Bozgush domain rotated and assumed their present geometry, the bounding faults would have come closer together.

4.4. Regional Implications

According to our paleomagnetic and structural interpretations of the Qosha Dagh and Bozgush region, deformation in NW Iran occurred in at least two phases since the Eocene. The exact timing of the rotations is imprecise, as the Eocene ages of the sampled rocks in our study only provide a maximum age constraint, and we did not sample younger units in this study. We hypothesize that the first phase of deformation was a regional ~40° clockwise rigid body rotation, which affected the block that Qosha Dagh and Bozgush are part of. The limits of this block are not entirely clear, due to the limited amount of paleomagnetic data from this structurally complex

region. While the 40° of regional rotation of the Qosha Dagh and Bozgush Mountains fits relatively well with the observed rotations in the Central Talesh (48°; Rezaeian et al., 2020), it is much larger than the rotations observed in both the north and south of the Talesh (~20°; Rezaeian et al., 2020; van der Boon et al., 2018). Furthermore, the Garmachay fault currently forms a boundary between the Bozgush and central Talesh, and these regions show differences in stress fields (Aflaki et al., 2021), indicating that they might not have behaved as a single rigid block. Paleomagnetic data from Miocene rocks (17–10 Ma) in the Mianeh basin, just south of the Bozgush Mountains, show no evidence for vertical axis rotations (Ballato et al., 2016). This could mean that either the limit of the rotated block lies just to the south of the Bozgush Mountains, or that rotation of the block took place after the Eocene, but before 17 Ma. We consider it most likely that at least a significant part of the rotations has taken place since the late Miocene, as all of the fault systems in the region are active until recently. This means that the Mianeh basin likely has a different tectonic history than the Bozgush region, and the South Bozgush fault forms the boundary between the two blocks, which is in line with the Global Positioning System (GPS) data of Djamour et al. (2011). The timing of the regional rotation is unconstrained, but we hypothesize that it is related to a tectonic phase that affected the nearby Alborz Mountains in the Miocene (Ballato et al., 2013; Mattei et al., 2017), and was a response to the Arabia-Eurasia collision, although we cannot exclude that all rotations are younger. We hypothesize that the regional rotation was coeval with the formation of the Lesser Caucasus-Talesh-Alborz orocline after the middle to late Miocene (Mattei et al., 2017), which wrapped around the rigid South Caspian Basin. The central Talesh might have moved with the Qosha Dagh and Bozgush, and the additional rotation of the central Talesh was accommodated during later stages of deformation, possibly through activity on the Garmachay fault. The block is likely bound by the Tabriz fault in the southwest and the Aras fault in the northwest.

The second deformation phase caused additional rotations that are confined to the eastern Bozgush domain. During this phase, an extra set of faults formed that cut the eastern Bozgush domain into small NNE-SSW elongated fault bounded blocks. The additional (~40°) rotations observed in this domain are local rotations and affected domino-style blocks. The timing of this phase is constrained by cross-cutting of the Tabriz fault and North and South Bozgush faults by the NNE-SSW faults. The Tabriz fault has been estimated to have been active since around 4 Ma (late Pliocene), and has an estimated offset of around 17 km (Mesbahi et al., 2016). The NNE-SSW fault set is conjugate to the right-lateral Tabriz fault, and fault activity is ascribed to the Holocene by Faridi et al. (2017). A post 4 Ma age for the fault set leads to a minimum estimate of rotation rates of 10°/Myr. Similarly high rotation rates (35°/0.9 Myr) have been reported from California (Johnson et al., 1983). A Holocene age for the rotations would yield unrealistic rotation rates, and we thus hypothesize that the sinistral fault set already developed possibly during the Pliocene. Either way, rotation rates in the Bozgush region are higher than in other parts of Iran (Mattei et al., 2012).

The largest rotations we observe, in the eastern Bozgush domain, coincide with the largest change in the orientation of the stress field in NW Iran, where three crustal blocks interact; the Persian block, the Central Iran block and the Talesh block (Aflaki et al., 2021). Our rotations fit well with a model in which the crust in NW Iran is trapped between several large rigid blocks, as hypothesized by Solaymani Azad et al. (2019b), and the Tabriz fault cannot propagate easily toward the east (Aflaki et al., 2021). The eastern Bozgush domain essentially gets trapped, and the domino-style faults develop to accommodate further deformation, ultimately caused by ongoing Arabia-Eurasia convergence.

Our new paleomagnetic data substantiate the claim of Djamour et al. (2011), who suggested that the Bozgush Mountains are structurally more complex than a simple pop-up structure. Saber et al. (2018) note that uplift rates in the eastern Bozgush are much slower than in the western Bozgush mountains, and the western Bozgush Mountains are currently more tectonically active. This could mean that NNE-SSW sinistral strike-slip fault-regime is propagating, and faults might develop further to the western side of the Bozgush Mountains in the future. While our paleomagnetic data do not show counter-clockwise rotation of the eastern Bozgush, as hypothesized by Faridi et al. (2017), they substantiate the claim that the NNE-SSW striking sinistral faults in the Bozgush region are major players in regional deformation (Faridi et al., 2017).

In the context of current deformation in the region, a contentious issue arises from the discrepancy between compressional-extensional deformation characterized by strike-slip faults with reverse components and the extensional deformation proposed by Djamour et al. (2011) based on GPS velocities. Recent earthquakes in the region predominantly exhibit pure strike-slip faulting or strike-slip faulting with reverse components (Solaymani Azad et al., 2015). However, Djamour et al. (2011) argue that their data is too scarce to definitively determine the

driver of the north-south extension in the region. Therefore, it is possible that the detected north-south extension is a local phenomenon or an artifact due to inadequate distribution of GPS stations. Nevertheless, the ultimate driver of the deformation, fault activity and rotation in NW Iran is the Arabia-Eurasia collision, and further northwards convergence of the Arabian plate along the Bitlis-Zagros suture zone. The inception of the collision took place during the late Eocene (Koshnaw et al., 2021), and by the late Miocene the intensity of deformation and northwards convergence of the Arabian plate increased (McQuarrie and van Hinsbergen, 2013). The Arabia-Eurasia collision and ongoing convergence have resulted in strong, mostly clockwise rotations in NW Iran. We show that shortening is not accommodated uniformly, and a full reconstruction of the tectonic history of NW Iran is complex and requires a careful consideration of all the strike-slip faults in the region, as well as more paleomagnetic data of different blocks and units of different ages. Particularly paleomagnetism on Miocene and younger units can aid in constraining timing and magnitude of vertical axis rotations and reconstructing the tectonic evolution of Northwest Iran.

5. Conclusions

We obtained paleomagnetic results from 127 sites of Eocene volcanic rocks along two transects of the Bozgush Mountains and one transect of the Qosha Dagh Mountains in northwest Iran. Our results indicate that northwest Iran has undergone a regional 40° clockwise rotation since the Eocene. Furthermore, there is a significant difference in rotations between the east and west Bozgush domains, and the ongoing Arabia-Eurasia convergence affects the western and eastern domains differently. The eastern Bozgush domain was affected by a secondary, local clockwise rotation phase of an additional 40°, resulting in a total CW rotation of around 80° in the eastern Bozgush domain. The additional clockwise rotations in the eastern Bozgush domain are accommodated by a set of NNE-SSW striking sinistral fault bounded domino-style rotating blocks, which have an estimated offset of 1–3 km. Total shortening accommodated by these domino-style faults is estimated at around 4 km. These faults are currently seismically active, and thus form a significant seismic hazard.

Global Research Collaboration

This research is the result of a long-standing collaboration between the Institute for Advanced Studies in Basic Sciences (Zanjan, Iran) and Utrecht University (Utrecht, The Netherlands) that focuses on constraining closure of the Neotethys Ocean and collision of Arabia with Eurasia during the Cenozoic. Co-authorship follows the Vancouver recommendations.

Conflict of Interest

The authors declare no conflicts of interest relevant to this study.

Data Availability Statement

We provide online supplementary information in the form of an appendix. Data Set S1 contains all GPS data of sites (in decimal degrees, geodetic datum WGS84) as a .kmz file (*Sites*.kmz), Data Set S2 contains the paleomagnetic data including all vector interpretations per site in the *site*.col files, and Data Set S3 averages per site for each locality as *locality.pub* files for the web portal Paleomagnetism.org. Data is also available in Zenodo (Niknam et al., 2024 [Dataset]).

Acknowledgments
AvdB. acknowledges financial support from the Research Council of Norway through its Centers of Excellence scheme, project number 332523 (PHAB), as well as project number 334622 (Young Talent scheme, project PANDA). AvdB. benefited from discussions with Torgeir Andersen. MR. acknowledges funding from the Ministry of Energy (Sabalan geothermal project number 89/83) and IASBS. We thank Conall Mac Niocaill, Massimo Mattei, one anonymous reviewer and associate editor Augusto Rapalini for comments that have improved this manuscript.

References

Aflaki, M., Shabanian, E., Sahami, S., & Arshadi, M. (2021). Evolution of the stress field at the junction of Talesh – Alborz – Central Iran during the past 5 Ma: Implications for the tectonics of NW Iran. *Tectonophysics*, *821*, 229115. https://doi.org/10.1016/j.tecto.2021.229115

Amidi, M., Alavi Tehrani, N., Lotfi, M., Bordet, P., Haghipour, A., Sabzehei, M., et al. (1978). *Geological Quadrangle Map of Iran, No C3 Mianeh, 1: 250.000 series*. Geological Survey of Iran.

Asadian, O., Amini-Fazl, A., & Khodabandeh, A. (1993). Geological Map of Iran, 1:100.000 series, Sheet 5465 Torkamanchay-Qarachaman.

Asiabanha, A., Ghasemi, H., & Meshkin, M. (2009). Paleogene continental-arc type volcanism in North Qazvin, North Iran: Facies analysis and geochemistry. *Neues Jahrbuch für Mineralogie, Abhandlungen*, *186*(2), 201–214. https://doi.org/10.1127/0077-7757/2009/0144

Ballato, P., Cifelli, F., Heidarzadeh, G., Ghassemi, M. R., Wickert, A. D., Hassanzadeh, J., et al. (2016). Tectono-sedimentary evolution of the northern Iranian Plateau: Insights from middle-late Miocene foreland-basin deposits. *Basin Research*, *1*(4), 1–30. https://doi.org/10.1017/CBO9781107415324.004

Ballato, P., Stockli, D. F., Ghassemi, M. R., Landgraf, A., Strecker, M. R., Hassanzadeh, J., et al. (2013). Accommodation of transpressional strain in the Arabia-Eurasia collision zone: New constraints from (U-Th)/He thermochronology in the Alborz Mountains, North Iran. *Tectonics*, *32*, 1–18. https://doi.org/10.1029/2012TC003159

Behruzi, A., & Amini Azar, R. (1992). Geological Map of Iran 1:100,000 series, Sheet 5525 Sarab.
Berberian, M. (1997). Seismic sources of the Transcaucasian historical earthquakes. In *Historical and prehistorical earthquakes in the Caucasus*. In *NATO science partnership subseries* (pp. 233–311). Springer.
Berberian, M., & Arshadi, S. (1976). On the evidence of the youngest activity of the North Tabriz fault and the seismicity of Tabriz city. *Geological Survey of Iran Report*, *39*, 397–418.
Biggin, A. J., van Hinsbergen, D. J. J., Langereis, C. G., Straathof, G. B., & Deenen, M. H. L. (2008). Geomagnetic secular variation in the Cretaceous Normal Superchron and in the Jurassic. *Physics of the Earth and Planetary Interiors*, *169*(1–4), 3–19. https://doi.org/10.1016/j.pepi.2008.07.004
Butler, R. F. R. F. (1992). *Paleomagnetism: Magnetic domains to geologic terranes*. Blackwell Scientific Publications.
Cogné, J. P., Halim, N., Chen, Y., & Courtillot, V. (1999). Resolving the problem of shallow magnetizations of Tertiary age in Asia: Insights from paleomagnetic data from the Qiangtang, Kunlun, and Qaidam blocks (Tibet, China), and a new hypothesis. *Journal of Geophysical Research*, *104*(B8), 17715–17734. https://doi.org/10.1029/1999JB900153
Copley, A., Faridi, M., Ghorashi, M., Hollingsworth, J., Jackson, J., Nazari, H., et al. (2014). The 2012 August 11 Ahar earthquakes: Consequences for tectonics and earthquake hazard in the Turkish-Iranian plateau. *Geophysical Journal International*, *196*(1), 15–21. https://doi.org/10.1093/gji/ggt379
Copley, A., & Jackson, J. (2006). Active tectonics of the Turkish-Iranian Plateau. *Tectonics*, *25*(6), 1–19. https://doi.org/10.1029/2005tc001906
Deenen, M. H. L., Langereis, C. G., van Hinsbergen, D. J. J., & Biggin, A. J. (2011). Geomagnetic secular variation and the statistics of palaeomagnetic directions. *Geophysical Journal International*, *186*(2), 509–520. https://doi.org/10.1111/j.1365-246X.2011.05050.x
Deenen, M. H. L., Langereis, C. G., van Hinsbergen, D. J. J., & Biggin, A. J. (2014). Erratum to Geomagnetic secular variation and the statistics of palaeomagnetic directions [Geophysical Journal International, 186, (2011) 509–520]. *Geophysical Journal International*, *197*(1), 643. https://doi.org/10.1093/gji/ggu021
Djamour, Y., Vernant, P., Nankali, H. R., & Tavakoli, F. (2011). NW Iran-eastern Turkey present-day kinematics: Results from the Iranian permanent GPS network. *Earth and Planetary Science Letters*, *307*(1–2), 27–34. https://doi.org/10.1016/j.epsl.2011.04.029
Faridi, M., Burg, J.-P., Nazari, H., Talebian, M., & Ghorashi, M. (2017). Active faults pattern and interplay in the Azerbaijan Region (NW Iran). *Geotectonics*, *51*(4), 428–437. https://doi.org/10.1134/S0016852117040033
Garfunkel, Z., & Ron, H. (1985). Block rotation and deformation by strike-slip faults, 2. The properties of a type of macroscopic discontinuous deformation. *Journal of Geophysical Research*, *90*(B10), 8589–8602. https://doi.org/10.1029/JB090iB10p08589
Ghods, A., Shabanian, E., Bergman, E., Faridi, M., Donner, S., Mortezanejad, G., & Aziz-Zanjani, A. (2015). The Varzaghan-Ahar, Iran, earthquake Doublet (Mw 6.4, 6.2): Implications for the geodynamics of northwest Iran. *Geophysical Journal International*, *203*(1), 522–540. https://doi.org/10.1093/gji/ggv306
Gholami, E., Ahmadi, A., Khatib, M., & Madanipour, S. (2021). Low temperature thermochronometry and structural constrains on evolution pattern of the Bozgoosh and Chehel-Nour Mountains intersection, NW Iran (in Persian). *Scientific Quarterly Journal of Geosciences*, *31*, 123–138. https://doi.org/10.22071/gsj.2021.257804.1864
Heidari, S., Shabani, A. A. T., Hassanpour, S., & Maghdour-Mashhour, R. (2022). Petrology of the Paleogene shoshonitic volcanism in north Sarab area, NW Iran: Geochemical, Ar-Ar dating and Sr-Nd-Pb isotopic constraints. *Journal of Asian Earth Sciences X*, *8*, 100109. https://doi.org/10.1016/j.jaesx.2022.100109
Hessami, K., Pantosi, D., Tabassi, H., Shabanian, E., Abbassi, M.-R., Feghhi, K., & Solaymani, S. (2003). Paleoearthquakes and slip rates of the North Tabriz fault, NW Iran: Preliminary results. *Annals of Geophysics*, *46*(5), 903–915.
Isik, V., Saber, R., & Caglayan, A. (2021). November 08, 2019 Turkmanchay earthquake (Mw: 5.9) in NW Iran: An assessment of the earthquake using DInSAR time-series and field evidence. *Natural Hazards*, *105*(3), 3013–3037. https://doi.org/10.1007/s11069-020-04439-1
Jackson, J. (1992). Partitioning of strike-slip and convergent motion between Eurasia and Arabia in Eastern Turkey and the Caucasus. *Journal of Geophysical Research*, *97*(B9), 12471–12479. https://doi.org/10.1029/92jb00944
Johnson, N. M., Officer, C. B., Opdyke, N. D., Woodard, G. D., Zeitler, P. K., & Lindsay, E. H. (1983). Rates of late Cenozoic tectonism in the Vallecito–Fish Creek basin, western Imperial Valley, California. *Geology*, *11*, 664–667. https://doi.org/10.1130/0091-7613(1983)11<664:ROLCTI>2.0.CO;2
Kirschvink, J. L. (1980). The least-squares line and plane and the analysis of palaeomagnetic data. *Geophysical Journal International*, *62*(3), 699–718. https://doi.org/10.1111/j.1365-246X.1980.tb02601.x
Koshnaw, R., Schlunegger, F., & Stockli, D. (2021). Detrital zircon provenance record of the Zagros mountain building from the Neotethys obduction to the Arabia-Eurasia collision, NW Zagros fold-thrust belt, Kurdistan region of Iraq. *Solid Earth*, *12*(11), 2479–2501. https://doi.org/10.5194/se-12-2479-2021
Koymans, M. R., van Hinsbergen, D. J. J., Pastor-Galán, D., Vaes, B., & Langereis, C. G. (2020). Towards FAIR paleomagnetic data management through paleomagnetism.org 2.0. *Geochemistry, Geophysics, Geosystems*, *21*(2), 1–7. https://doi.org/10.1029/2019GC008838
Luyendyk, B. P., Kamerling, M. J., & Terres, R. (1980). Geometric model for Neogene crustal rotations in southern California. *GSA Bulletin*, *91*(4), 211–217. https://doi.org/10.1130/0016-7606(1980)91<211:GMFNCR>2.0.CO;2
Mahdavi, M. A., & Amini Fazl, A. (1988). Geological map of Iran 1:100,000 series - Sheet 5466, Ahar. Geological map of Iran 1:100,000 series.
Mattei, M., Cifelli, F., Alimohammadian, H., & Rashid, H. (2020). The role of active strike-slip faults and opposite vertical axis rotations in accommodating Eurasia-Arabia shortening in central Iran. *Tectonophysics*, *774*, 228243. https://doi.org/10.1016/j.tecto.2019.228243
Mattei, M., Cifelli, F., Alimohammadian, H., Rashid, H., Winkler, A., & Sagnotti, L. (2017). Oroclinal bending in the Alborz Mountains (Northern Iran): New constraints on the age of South Caspian subduction and extrusion tectonics. *Gondwana Research*, *42*, 13–28. https://doi.org/10.1016/j.gr.2016.10.003
Mattei, M., Cifelli, F., Muttoni, G., Zanchi, A., Berra, F., Mossavvari, F., & Eshraghi, S. A. (2012). Neogene block rotation in central Iran: Evidence from paleomagnetic data. *Bulletin of the Geological Society of America*, *124*(5–6), 943–956. https://doi.org/10.1130/B30479.1
McFadden, P. L., & McElhinny, M. W. (1988). The combined analysis of remagnetization circles and direct observations in palaeomagnetism. *Earth and Planetary Science Letters*, *87*(1–2), 161–172. https://doi.org/10.1016/0012-821x(88)90072-6
McQuarrie, N., & van Hinsbergen, D. J. J. (2013). Retrodeforming the Arabia-Eurasia collision zone: Age of collision versus magnitude of continental subduction. *Geology*, *41*(3), 315–318. https://doi.org/10.1130/G33591.1
Mesbahi, F., Mohajjel, M., & Faridi, M. (2016). Neogene oblique convergence and strain partitioning along the North Tabriz Fault, NW Iran. *Journal of Asian Earth Sciences*, *129*, 191–205. https://doi.org/10.1016/j.jseaes.2016.08.010
Mullender, T. A. T., Frederichs, T., Hilgenfeldt, C., de Groot, L. V., Fabian, K., & Dekkers, M. J. (2016). Automated paleomagnetic and rock magnetic data acquisition with an in-line horizontal "2G" system. *Geochemistry, Geophysics, Geosystems*, *17*(9), 3546–3559. https://doi.org/10.1002/2016GC006436

Mullender, T. A. T., van Velzen, A. J., & Dekkers, M. J. (1993). Continuous drift correction and separate identification of ferrimagnetic and paramagnetic contributions in thermomagnetic runs. *Geophysical Journal International*, *114*(3), 663–672. https://doi.org/10.1111/j.1365-246X.1993.tb06995.x

Niknam, A., van der Boon, A., Rezaeian, M., Kaymakcı, N., & Langereis, C. (2024). Paleomagnetic data of the Bozgush Mountains [Dataset]. https://doi.org/10.5281/zenodo.12795515

Nur, A., Ron, H., & Scotti, O. (1986). Fault mechanics and the kinematics of block rotations. *Geology*, *14*(9), 746–749. https://doi.org/10.1130/0091-7613(1986)14<746:FMATKO>2.0.CO;2

Onderdonk, N. W. (2005). Structures that accommodated differential vertical axis rotation of the western Transverse Ranges, California. *Tectonics*, *24*(4), TC4018. https://doi.org/10.1029/2004TC001769

Reilinger, R., McClusky, S., Vernant, P., Lawrence, S., Ergintav, S., Cakmak, R., et al. (2006). GPS constraints on continental deformation in the Africa-Arabia-Eurasia continental collision zone and implications for the dynamics of plate interactions. *Journal of Geophysical Research*, *111*(B5), B05411. https://doi.org/10.1029/2005JB004051

Rezaeian, M., Kuijper, C. B., van der Boon, A., Pastor-Galán, D., Cotton, L. J., Langereis, C. G., & Krijgsman, W. (2020). Post-Eocene coupled oroclines in the Talesh (NW Iran): Paleomagnetic constraints. *Tectonophysics*, *786*, 228459. https://doi.org/10.1016/j.tecto.2020.228459

Rizza, M., Vernant, P., Ritz, J. F., Peyret, M., Nankali, H., Nazari, H., et al. (2013). Morphotectonic and geodetic evidence for a constant slip-rate over the last 45 kyr along the Tabriz fault (Iran). *Geophysical Journal International*, *193*(3), 1083–1094. https://doi.org/10.1093/gji/ggt041

Saber, R., Caglayan, A., & Isik, V. (2018). Relative tectonic activity assessment and kinematic analysis of the North Bozgush fault Zone, NW Iran. *Journal of Asian Earth Sciences*, *164*, 219–236. https://doi.org/10.1016/j.jseaes.2018.06.023

Saber, R., Isik, V., & Caglayan, A. (2021). Structural styles of the Aras fault zone with implications for a transpressive fault system in NW Iran. *Journal of Asian Earth Sciences*, *207*, 104655. https://doi.org/10.1016/j.jseaes.2020.104655

Si, J., & Van der Voo, R. (2001). Too-low magnetic inclinations in Central Asia: An indication of a long-term Tertiary non-dipole field? *Terra Nova*, *13*(6), 471–478. https://doi.org/10.1046/j.1365-3121.2001.00383.x

Solaymani Azad, S., Esmaeili, C., Roustai, M., Vajedian, S., Khosh Zare, T., Rajab Zadeh, H. R., et al. (2019a). The geological features of the Torkmanchai NW Iran Earthquake on November 8, 2019 (Mw=5.9).

Solaymani Azad, S., Nemati, M., Abbassi, M.-R., Foroutan, M., Hessami, K., Dominguez, S., et al. (2019b). Active-couple indentation in geodynamics of NNW Iran: Evidence from synchronous left- and right-lateral co-linear seismogenic faults in western Alborz and Iranian Azerbaijan domains. *Tectonophysics*, *754*, 1–17. https://doi.org/10.1016/j.tecto.2019.01.013

Solaymani Azad, S., Philip, H., Dominguez, S., Hessami, K., Shahpasandzadeh, M., Foroutan, M., et al. (2015). Paleoseismological and morphological evidence of slip rate variations along the North Tabriz fault (NW Iran). *Tectonophysics*, *640–641*, 20–38. https://doi.org/10.1016/j.tecto.2014.11.010

Tauxe, L., Butler, R. F., Voo, R., & Banerjee, S. K. (2010). *Essentials of paleomagnetism*. University of California Press.

Tauxe, L., & Watson, G. S. (1994). The fold test: An Eigen analysis approach. *Earth and Planetary Science Letters*, *122*(3–4), 331–341. https://doi.org/10.1016/0012-821x(94)90006-x

Torsvik, T. H., van der Voo, R., Preeden, U., Mac Niocaill, C., Steinberger, B., Doubrovine, P. V., et al. (2012). Phanerozoic polar wander, palaeogeography and dynamics. *Earth-Science Reviews*, *114*(3–4), 325–368. https://doi.org/10.1016/j.earscirev.2012.06.002

Valerio, E., Manzo, M., Casu, F., Convertito, V., De Luca, C., Manunta, M., et al. (2020). Seismogenic source model of the 2019, Mw 5.9, East-Azerbaijan Earthquake (NW Iran) through the Inversion of Sentinel-1 DInSAR measurements. *Remote Sensing*, *12*(8), 1–14. https://doi.org/10.3390/RS12081346

van der Boon, A., Kuiper, K. F., Villa, G., Renema, W., Meijers, M. J. M., Langereis, C. G., et al. (2017). Onset of Maikop sedimentation and cessation of Eocene arc volcanism in the Talysh Mountains, Azerbaijan. *Geological Society, London, Special Publications*, *428*(1), 145–169. https://doi.org/10.1144/sp428.3

van der Boon, A., van Hinsbergen, D. J. J., Rezaeian, M., Gürer, D., Honarmand, M., Pastor-Galán, D., et al. (2018). Quantifying Arabia–Eurasia convergence accommodated in the Greater Caucasus by paleomagnetic reconstruction. *Earth and Planetary Science Letters*, *482*, 454–469. https://doi.org/10.1016/j.epsl.2017.11.025

van Velzen, A. J., & Zijderveld, J. D. A. (1995). Effects of weathering on single-domain magnetite in Early Pliocene marine marls. *Geophysical Journal International*, *121*(1), 267–278. https://doi.org/10.1111/j.1365-246X.1995.tb03526.x

Vernant, P., Nilforoushan, F., Hatzfeld, D., Abbassi, M. R., Vigny, C., Masson, F., et al. (2004). Present-day crustal deformation and plate kinematics in the Middle East constrained by GPS measurements in Iran and northern Oman. *Geophysical Journal International*, *157*(1), 381–398. https://doi.org/10.1111/j.1365-246X.2004.02222.x

Watson, A. R., Elliott, J. R., Lazecký, M., Maghsoudi, Y., McGrath, J. D., & Walters, R. J. (2024). An InSAR-GNSS velocity field for Iran. *Geophysical Research Letters*, *51*(10), e2024GL108440. https://doi.org/10.1029/2024GL108440

Westphal, M. (1993). Did a large departure from the geocentric axial dipole hypothesis occur during the Eocene? Evidence from the magnetic polar wander path of Eurasia. *Earth and Planetary Science Letters*, *117*(1–2), 15–28. https://doi.org/10.1016/0012-821X(93)90114-O

Yang, J., Xu, C., & Wen, Y. (2020). The 2019 Mw 5.9 Torkaman chay earthquake in Bozgush Mountain, NW Iran: A buried strike-slip event related to the sinistral Shalgun-Yelimsi fault revealed by InSAR. *Journal of Geodynamics*, *141–142*, 101798. https://doi.org/10.1016/j.jog.2020.101798

Zijderveld, J. D. A. (1967). AC demagnetization of rocks: Analysis of results. In D. W. Collinson & K. M. Creer (Eds.), *Methods in paleomagnetism* (pp. 254–286). Elsevier.

Zuza, A. V., & Yin, A. (2016). Continental deformation accommodated by non-rigid passive bookshelf faulting: An example from the Cenozoic tectonic development of northern Tibet. *Tectonophysics*, *677–678*, 227–240. https://doi.org/10.1016/j.tecto.2016.04.007